Modeling of a-Si:H n-i-p detectors

by

Tsu Chiang Chuang

A thesis
presented to the University of Waterloo
in fulfilment of the
thesis requirement for the degree of
Master of Applied Science
in
Electrical and Computer Engineering

Waterloo, Ontario, Canada, 2007

I hereby declare that I am the sole author of this thesis. This is a true copy of the thesis, including any required final revisions, as accepted by my examiners.

I understand that my thesis may be made electronically available to the public.

Abstract

The widespread use of hydrogenated amorphous silicon (a-Si:H) devices prompted the need for models to identify challenges and solutions early on in the design process. Hydrogenated amorphous silicon photodiodes are commonly used as sensors in large area scanners. It is possible to describe a-Si:H n-i-p photodiodes using an empirical model, which this dissertation presents.

Segmented a-Si:H n-i-p photodiodes of varying sizes were fabricated via plasma enhanced chemical vapor deposition. The dark current-voltage characteristics were then measured at different temperatures. The capacitance and the quantum efficiency of the devices were also characterized.

Using simple semiconductor device equations and the observed empirical behavior, a model is built with a series of parameterized equations. The forward bias current characteristics are represented by the weighted sum of a low bias exponential relationship and a high bias power law relationship. The reverse bias current is modeled as the sum of the bulk thermal component and the edge leakage component. A linear bias dependent equation is used to represent the diode capacitance and a fourth order polynomial is used to model the quantum efficiency. The devices are characterized and the parameters are extracted from the empirical results. Good agreement has been obtained by comparing the results of the proposed model with the experimental results.

Acknowledgements

First of all, I would like to express my sincerest gratitude to my supervisors, Dr. Nathan, Dr. Rowlands, and Dr. Shen, for giving me the opportunities and the constant support necessary for me to complete my thesis. Their expertise, guidance, understanding and patience have considerably enriched my graduate experience. I am honored to have Dr. Striakhilev and Dr. Sazonov as my readers. I will also like to thank Gregory Heiler and Timothy Tredwell from Eastman Kodak™for their constant feedback and discussion through the course of my research. Their comments and insights have provided a fresh perspective into the topic. I am indebted to Dr. Vygranenko and Dr. Kim for providing me with the numerous samples from which I could extract my data. I doubt I can ever express my full appreciation for their help. A very special thanks also goes out to Dr. Hamel for his generous allowance in using the temperature controlled probe station. To my fellow laboratory and graduate friends in the Giga2Nano group, my thanks goes to them for being there as role models and friends. The weekly outings and discussions have kept me sane through the rigorous program. I would also like to thank my family and friends for their constant encouragement and support. Finally, I would like to recognize that this research would not have been possible without the financial assistance of the Eastman Kodak™, NSERC, the University of Waterloo Graduate Studies, and the Department of Electrical and Computer Engineering at the University of Waterloo, and express my thanks to those agencies.

Contents

List of Tables

List of Figures

Chapter 1

Introduction

Amorphous materials are a very viable and attractive alternative for semiconductor devices due to their lower cost and large area capabilities. Solar cells [11], photodetectors [12], thin-film transistors (TFTs) [13], light-emitting diodes (LEDs) [14], and memory switch devices [15] are among some of the many devices made from hydrogenated amorphous silicon. The widespread use of amorphous materials has prompted the need for the basic understanding of their physical characteristics. If one is to design a device made of such a material, it would be beneficial to derive a model to determine its performance and any possible design issues before mass production.

1.1 Problem Description and Motivation

Models are theoretical constructs that use variables and the relations between them to represent something. The Bohr model of the atom, the Gaussian-chain model

of a polymer, the double helix model of deoxyribonucleic acid (DNA) are some of the common models used nowadays in the scientific community [16]. Models are constructed to help researchers understand a complex problem, often by making assumptions that are known to be either false or incomplete. There are many different types of models, each with its own strengths and weaknesses. Models are so pervasive that there may be more than one model explaining the same physical phenomenon and in the worst case they might even contradict each other.

The problem of multiple models also affects amorphous materials. For a-Si:H n-i-p photodiodes, the literature reports an assortment of models, each model validated by fundamental equations and empirical results. However, some of these models do not agree with each other. Each model aims at explaining some part of the complex nature of hydrogenated amorphous silicon [17] [18] [19] [20] [21] [22] [23] [24] [25]. Some of these models are purely theoretical, while others are empirical-based. Empirical models can be derived more easily for established processes, but they usually lack the scope necessary to explain the underlining physics. Theoretical models on the other hand tend to be more complete, but are more complex and harder to derive. Despite the drawbacks observed in empirical models, they are sometimes preferred over theoretical models since they can be derived and simulated faster. In addition, by using a simpler model with an analytical expression rather than a numerical one, large complex systems can be simulated with fewer computing resources.

Empirical models are sometimes referred to as models of data [26]. An empirical model is essentially a corrected, rectified, idealized version of the data gained from immediate observation, also known as a raw data. In general, one performs data reduction and curve fitting on the gathered data to derive the model [16]. Data

reduction involves the exclusion of errors or data from faulty observations. As implied by its name, curve fitting is the act of finding the trend in the observed data by drawing a smooth curve through the set of points. However, the construction of a data model is not as simple as it sounds. It requires the use of statistical techniques and raises some methodological questions. Some of these questions include how to determine which points are noise, or how to fit a curve through a clean set of data. The former problem is closely related on how the experiment is conducted. By minimizing the number of noise sources, good raw data can be obtained and no or very little data reduction needs to be done. The latter issue is the curve fitting problem, where the data does not indicate what form the fitted curve should take. The curve fitting problem can be solved mainly with background theory, simplicity, prior probabilities, or a combination of all three. Some researchers state that by using the Akaike information criterion [27], data will infer a curve shape that maximizes predictive accuracy [28]. In short, although there is no set methodology on how a model can be derived [29], by performing several iterations of data gathering, data reduction, and curve fitting an empirical model can be derived.

The aim of this dissertation is to present the idea on how an empirical model for an a-Si:H p-i-n or n-i-p photodiode can be extracted from theoretical equations. The parameters and model equations found here might be very specific to the processes and geometries used at the University of Waterloo Giga2Nano Laboratory, but the methodology hopefully will be general enough that it can be applied to other devices regardless of fabrication restrictions.

1.2 Thesis Organization

To present the model building methodology in a systematic manner, this dissertation is organized into three main areas. The first part, which includes Chapters 1 to 3, provides the general background necessary to the formulation of the model. Chapter 4 presents the details of the model. Chapter 5 follows by implementing and validating the model. Finally, Chapter 6 concludes this thesis.

Although the proposed model is an empirical one, it still depends on the physics related to the material. Therefore, a good understanding of the material properties is important. Chapter 2 aims at providing the necessary background material regarding hydrogenated amorphous silicon (a-Si:H). The relevant physical properties of a-Si:H are summarized, including the electronic density of states, metastability, carrier transport and photoconductivity.

Building on the groundwork established in Chapter 2, Chapter 3 introduces the n-i-p structure. The mode of operation of the photodiode is explained. Then, other characteristic parameters related to its performance are described. These factors include its capacitance, metastability, quantum efficiency, trap state release, operational temperature and noise.

The model of the n-i-p diode is examined in Chapter 4. In this chapter the fundamental equations describing each component of the diode is presented.

Chapter 5 validates the suggested model. The test setup as well as the samples tested are described. The experimental results and extraction methodology are presented.

Chapter 2

Hydrogenated Amorphous Silicon

Hydrogenated amorphous silicon (a-Si:H) is a relatively new material. In the 1960s, non-hydrogenated amorphous silicon (a-Si) was studied when research was conducted on chalcogenides [1]. At that time, a-Si was made by sputtering or by thermal evaporation. a-Si was considered an impractical material due to its high defect density and inability to be doped. In 1969, Chittick et al. used glow discharge and silane (SiH_4) to produce the first hydrogenated amorphous silicon (a-Si:H) film [30]. The addition of hydrogen, hydrogenation, to a-Si improves its electronic properties by passivating the dangling bonds. The passivation of dangling bonds removes the electronic states within the band-gap and eliminates most of the trapping and recombination centers. Even with the observed improvement of photoconductivity and defect density, a-Si:H did not draw much interest at that time because the overall electronic quality was still far worse than that of its crystalline counterpart [31]. However, Le Comber et al., from the University of Dundee, reported the possibility of substitutional n-type or p-type doping in a-Si:H in 1975 [32]. Since then, a-Si:H has been heavily researched and various theories concerning its properties

presented.

This chapter provides the necessary a-Si:H background for modeling the photodiode. Section 2.1 introduces the advantages and structure of hydrogenated amorphous silicon. Then, Section 2.2 describes the density of states of a-Si:H and how it differs from standard crystalline silicon (c-Si). The concept of defects and metastability as it applies to a-Si:H will be covered in Section 2.3. Finally, electronic transport and photoconduction are explained in Sections 2.4 and 2.5.

2.1 Structure and General Characteristics

Hydrogenated amorphous silicon (a-Si:H) is a non-crystalline form of silicon. Non-crystalline semiconductors possess the same short-range order, but lack the long-range order of their crystalline counterpart. The short range order of amorphous materials means that for a given atom, the bond length and bond angle to its neighbors are the same as those of crystalline materials. However, the bond angles values deviate within 10 % after a few interatomic spacings [1]. A comparison between crystalline and amorphous silicon is shown in Figure 2.1. Despite their lack of long-range order, amorphous semiconductors generally have well-defined bond lengths, bond angles and coordinations. Coordination, the specific number of bonds an atom makes to its immediate neighboring atoms, is determined by Mott's "8-N" rule [33], where N is the number of valence electrons. For example, since silicon has four valence electrons, its optimal coordination is four. Usually the structure of amorphous semiconductors can be modeled using continuous random networks. The continuous random network model treats the structure of a covalently bonded amorphous material such that perfect connectivity is maintained among atoms but

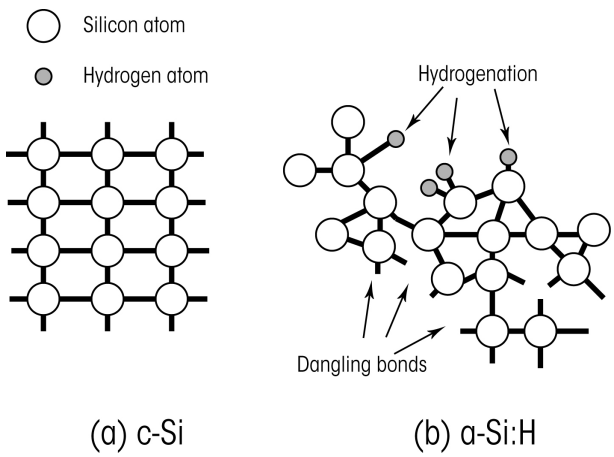

Figure 2.1: Illustration showing (a) c-Si atomic structure and (b) a-Si:H atomic structure.

the periodicity is not well-retained [1]. Some of the electronic properties of device grade a-Si:H are shown in Table 2.1.

As can be seen in Table 2.1, the electronic properties of amorphous materials are usually worse than crystalline materials due to the loss of long-range order. However, there are several advantages that make amorphous semiconductors attractive to large area electronics [34].

First, since the crystallinity of the material is not that critical of an issue in a-Si:H, large-area deposition are readily available for a-Si:H. This allows for the deployment of large arrays of devices. For example, the current maximum wafer size for a-Si:H is about 4 m^2, compared to 12" c-Si wafers that are around 0.072 m^2. Second, c-Si fabrication temperatures are lower bounded by the melting point of silicon using the Czochralski growth method and by the thermal oxidation process [35]. On the other hand, a-Si:H growth process can be done at temperatures below 450 °C using plasma enhanced chemical vapor deposition (PECVD), which allows for the

Table 2.1: Characteristics of device grade a-Si:H [1].

Parameter	Symbol	Value	Unit
Hydrogenation concentration	$[H]$	10	at. %
Optical band gap	E_μ	$1.7 - 1.8$	eV
Slope of conduction band-tail	E_{OC}	30	meV
Slope of valence band-tail	E_{OV}	50	meV
Defect density	N_D	10^{15}	cm^{-3}
Electron drift mobility	μ_n	1	$\mathrm{cm}^2\mathrm{V}^{-1}\mathrm{s}^{-1}$
Hole drift mobility	μ_p	0.003	$\mathrm{cm}^2\mathrm{V}^{-1}\mathrm{s}^{-1}$
Carrier diffusion length	λ_{Diff}	0.3	μm
Intrinsic a-Si:H Conductivity at 300 K	$\sigma_{intrinsic}$	10^{-11}	Ω^{-1} cm^{-1}
n+ a-Si:H Conductivity at 300 K	σ_{n+}	10^{-2}	Ω^{-1} cm^{-1}
p+ a-Si:H Conductivity at 300 K	σ_{p+}	10^{-3}	Ω^{-1} cm^{-1}

use of other materials such as plastics as substrates. Third, a-Si:H has very good optoelectronic properties, with an absorption length 200 times shorter than c-Si. a-Si:H bandgap is suitable for optical sensors and solar cells. The bandgap and the absorption spectrum can also be tuned by the alloying of a-Si:H with carbon or germanium. Fourth, since a-Si:H already has a high defect concentration of 10^{15} cm^{-3} to 10^{16} cm^{-3}, the adverse effects associated with radiation damage and background impurities are not as important as in cystalline materials. Fifth, the fabrication process of a-Si:H is compatible with standard silicon fabrication processes. As a matter of fact, a-Si:H films are generally grown by Plasma Enhanced Chemical Vapor Deposition (PECVD). This makes the adoption of a-Si:H by standard fabrication facilities a lot easier. A typical PECVD reactor is shown in Figure 2.2. Reactive gases are decomposed by plasma and are grown on a substrate.

The quality of the deposited a-Si:H layer depends on various deposition parameters, including: RF power, substrate temperature, gas composition, gas flow and

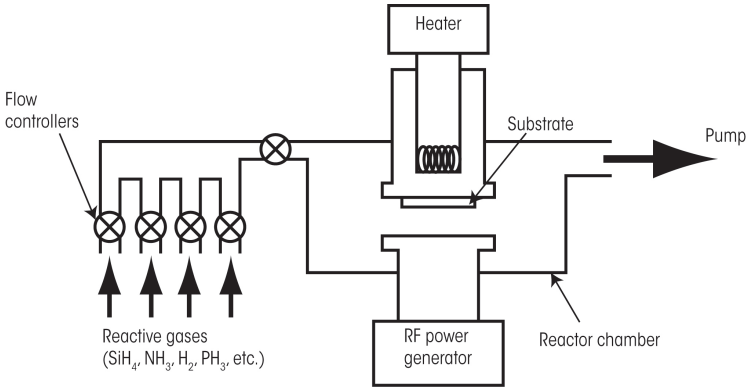

Figure 2.2: Schematic of a standard Plasma enhanced chemical vapor deposition chamber.

gas pressure. The RF power determines the film growth rate. The deposition temperature controls the chemical reactions on the growing surface. The composition of the gas determines the type of a-Si:H film grown. The gas flow rate controls the residence time of the gases in the reactor. The gas pressure determines the mean free path of the gas molecules, and it is usually around $0.1 \sim 1$ Torr [1].

As mentioned previously, hydrogenation is important in reducing the number of defects in a-Si. Hydrogen content decreases with increasing temperature and varies with radio frequency (RF) power [36]. Research literature reports that device quality a-Si:H films are grown at temperatures around 200 to 300 °C and at low RF power [1]. In addition, the deposition of a-Si can be further controlled by diluting silane with noble gases. The dilution of silane can be beneficial to the deposition of a-Si. However, silane should not be too diluted as it might cause columnar morphology which is also adverse to film quality [37]. The hydrogen concentration in device grade a-Si:H films is around 10 atomic %.

2.2 Electronic Density of States

The band gap, which is the separation between the top of the occupied valence band and the bottom of the empty conduction band, is one of the fundamental parameters of crystalline semiconductors. It is often described by the splitting of the bonding and anti-bonding states and is a consequence of the periodicity of the lattice.

The wave function of electronic states in c-Si can be derived by solving the Schrödinger equation with a periodic potential well. It can be described by the Bloch wave as:

$$\Psi(\overrightarrow{r}, \overrightarrow{k}) = u(\overrightarrow{r}, \overrightarrow{k})e^{i\overrightarrow{k}\cdot\overrightarrow{r}}, \tag{2.1}$$

where $\overrightarrow{k}$ is a three-dimensional space vector. The function $u(\overrightarrow{r}, \overrightarrow{k})$ describes the potential well periodic in $\overrightarrow{r}$ with the periodicity of the crystal lattice [38]. The wave function has a well-defined momentum $\overrightarrow{k}$ which extends throughout the crystal. Since a-Si:H lacks this periodicity, k-space cannot exist and the wave function cannot be expressed by the Bloch wave. However, the density of states is a valid description of electron states for both c-Si and a-Si:H [39].

There are many models in literature available to describe the distribution of density of states (DOS) in a-Si:H. The most common model used to describe the DOS of a-Si:H is the Mott-Davis-Street model shown in Figure 2.3. In contrast to the sharp band edges found in c-Si, the a-Si:H DOS has band-tails of localized states extending into the gap, caused by the lack of long range order. In an amorphous semiconductor, electrons may become localized, meaning that the wave function is confined to a small value rather than being extended. Anderson, who was the first to model electron localization, showed that if the average of the disordered poten-

tial experienced by electrons exceed a critical value, all the electron states in the material are localized [40]. At absolute zero (0 K), the mobility of elections above the mobility edge is finite, but the electrons below the mobility edge are immobile. In other words, at 0 K, the localized states do not contribute to conduction.

In the Mott-Davis-Street model, the band-tails are a few tenths of an eV, and the Fermi level is locked near the mid-gap by the defect levels. This model is favored over the Cohen-Fritzsche-Ovshinsky model, since it explains the doping found in a-Si:H [1]. The DOS of the valence band and conduction band can be measured by photoemission and inverse photoemission respectively [41].

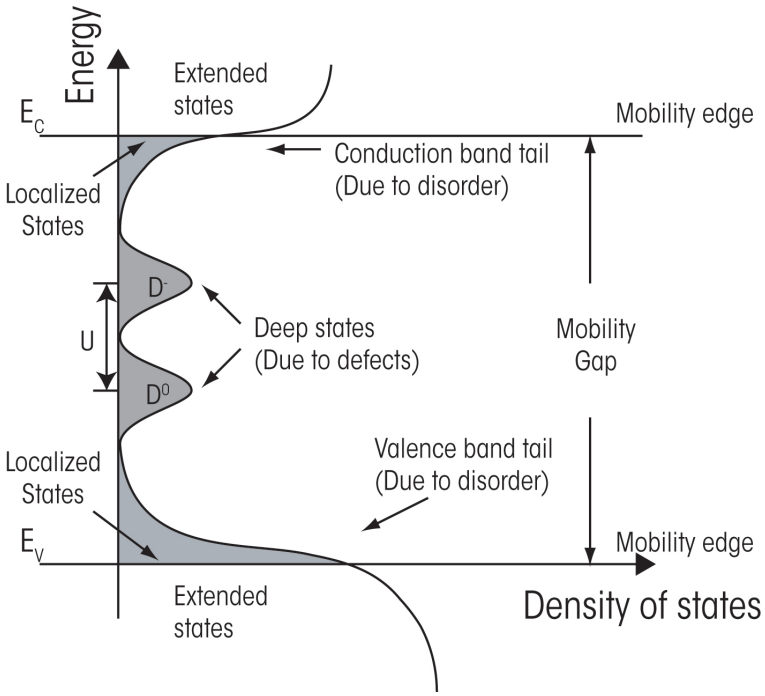

Figure 2.3: Mott-Davis-Street density of states model for a-Si:H.

The extended states of the conduction band and valence bands are separated from their respective tail states by their mobility edges E_C and E_V. The DOS

distributions for the conduction band tail and valence band-tail states are assumed to be single exponential functions of energy with their respective characteristic energies E_{OC} and E_{OV} and can be expressed as:

$$\begin{aligned} N_{ct}(E) &= N_{co}e^{-\frac{E_C-E}{E_{OC}}}, \\ N_{vt}(E) &= N_{vo}e^{-\frac{E}{E_{OV}}}, \end{aligned} \tag{2.2}$$

where E is the energy level measured from E_V, N_{co} and N_{vo} are the density of states at E_C and E_V respectively.

2.3 Defects and Metastability

The definition of defects differs for a-Si:H and c-Si. In c-Si, any deviation from the ordered structure, such as impurity atoms, vacancies, or interstitial atoms, is considered a defect. On the other hand, defects in a-Si:H are defined to be coordination defects, when an atom violates the Mott "8-N" rule.

Broken bonds or defects in a-Si:H have one unpaired electron, which occupy an energy level in the mid-gap. Due to the slight variations arising from the environment, there is a distribution of electron energies near the mid-gap. The defect states are usually modeled as Gaussian functions. This can be seen in Figure 2.3. Consequently, dangling bonds are the source of generation and recombination centers in the forbidden gap.

The dangling bonds have three possible charge states, namely the negatively charged D^- state which has an additional electron trapped, the neutral D^0 state which has its own electron, and the positively charged D^+ state which lacks an electron. The two electrons in a D^- state repel each other by the Coulomb force

and the energy levels are split by the so called correlation energy [1]. The splitting of the D^- and D^0 states due to the correlation energy U is also shown in Figure 2.3.

Defects can be temporarily created in a-Si:H whenever the Fermi level is driven away from its equilibrium position. This metastable phenomena can be caused by light [42] [43], doping [44], or electrical field [45]. Although hydrogen is beneficial in the passivation of dangling bonds in a-Si:H, it also contributes to the light induced degradation of a-Si:H, termed the Staebler-Wronski effect.

2.4 Carrier Transport

Carrier transport is defined as the movement of charge from one location to a different one in the semiconductor [34]. For c-Si, carrier transport occurs by electron and hole transport. Electron conduction is defined as the motion of electrons through the states in the conduction band. On the other hand, hole conduction is defined as the motion of electrons through the states in the valence band. Current density is a good figure of merit used to describe carrier transport. Current density depends on carrier concentration and carrier velocity. Carrier velocity is proportional to the electric field for low and medium fields. Then, the current density can be expressed as:

$$J = J_n + J_p = q(n\mu_n + p\mu_p)\overrightarrow{E} = \sigma\overrightarrow{E}, \tag{2.3}$$

where J_n, J_p, J are the electron, hole, and total current densities respectively. The values n, p, μ_p, μ_n, $\overrightarrow{E}$, σ refer to the electron concentration, hole concentration, electron mobility, hole mobility, electric field, and conductivity, respectively.

Carrier transport in a-Si:H shares many similarities to that of c-Si. Namely, electron drift mobility ($\mu_n \approx 1$ $cm^2V^{-1}s^{-1}$) is higher than hole drift mobility

($\mu_p \approx 10^{-2}$ cm^{2}V^{-1}s^{-1}) due to stronger hole trapping in the valence band. Therefore, electrons dominate the carrier transport in a-Si:H, giving rise to the name of "electronic transport". Due to scattering caused by the disorder in a-Si:H, the mobilities of electrons and holes are lower than that observed in c-Si [34]. Electrons can be transported through extended, localized or defect states, which is shown in Figure 2.4 [1].

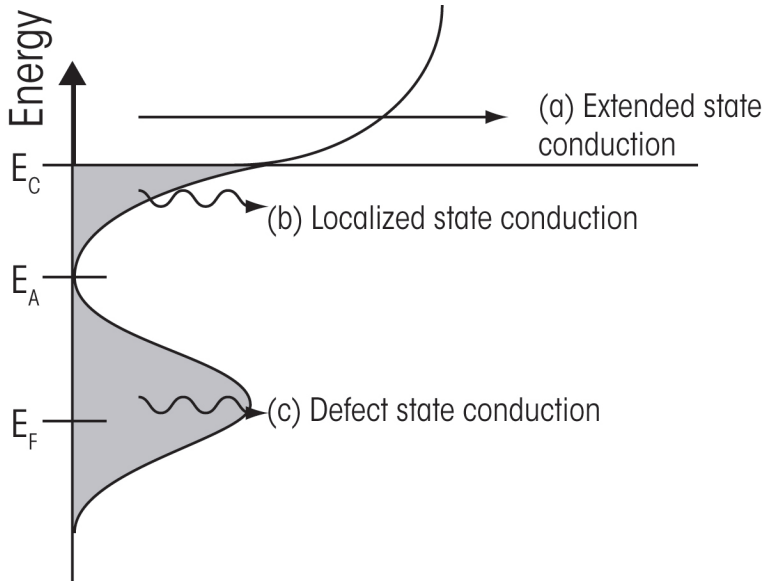

Figure 2.4: Schematic showing the three electronic transport mechanisms found in a-Si:H: (a)extended state conduction; (b)hopping in the band-tail; (c)hopping at E_F.

The extended state conductivity can be expressed as:

$$\sigma_{Extended} = \sigma_{\min} e^{-\left(\frac{E_C - E_F}{kT}\right)}, \tag{2.4}$$

where k, T, E_C, E_F are the Boltzmann's constant, temperature, conduction mobil-

ity edge, Fermi energy respectively. σ_{min} is defined as:

$$\sigma_{\min} = \frac{0.026q^2}{\hbar T}, \tag{2.5}$$

where q, $\hbar$, a are the elementary charge, the reduced Planck constant, and the average distance between atoms, respectively [30]. By assuming conduction is dominated by electrons, the conductivity for localized states can be expressed as:

$$\sigma_{Localized} = \sigma_1 e^{\left(-\frac{E_A - E_F + w_1}{kT}\right)}, \tag{2.6}$$

where E_A is the energy at which the conduction band-tail vanishes, as shown in Figure 2.4. The constant w_1 is the activation energy for hopping, which is temperature dependent. σ_1 is a prefactor which is much smaller than σ_{min}. Conductivity for carriers near the Fermi energy level hopping between deep localized states is:

$$\sigma_{Hopping} = \sigma_2 e^{\left(-\frac{w_2}{kT}\right)}, \tag{2.7}$$

where w_2 is the hopping energy for deep states and σ_2 is also a prefactor ($\sigma_2 \ll \sigma_1$).

At room temperature, electrons keep trapping and detrapping between the extended states above the mobility edge and localized states below the mobility edge. Therefore, the transport of charge carriers is trap-limited, and effective carrier mobility or drift mobility is lower than free carrier mobility. Since the trapping mechanism is temperature dependent, so is the drift mobility. At high temperatures, electronic transport through the extended states dominates, but the other two mechanisms also contribute depending on external parameters.

2.5 Photoconductivity

Photoconductivity is a phenomenon in which the conductivity of a material increases due to the absorption of an electro-magnetic radiation. In a-Si:H, electrons and holes can be optically excited to the band edges where they drift to the electrodes under the applied field. There are two types of photoconductivity: primary and secondary photoconductivity. If the contacts are blocking, then it is referred to as primary photoconductivity. On the other hand, if the contacts are leaky and the absorbed carriers are replaced by carriers injected from the other contact, then it is referred to as secondary photoconductivity [1]. Although primary photoconduction is usually the best structure for a light detector, it is the secondary photoconduction that is more commonly studied. The secondary photoconductivity can be modeled as:

$$\sigma_{ph} = Gq\left(\mu_{De}\tau_e + \mu_{Dh}\tau_h\right), \tag{2.8}$$

where G , q, $\mu_{De,Dh}$, and $\tau_{e,h}$ are the optical excitation rate, the elementary charge, the mobilities of free electrons and holes, and the recombination lifetime of the electrons and holes respectively. Assuming transport is dominated by electrons, Equation 2.8 can be expressed as:

$$\sigma_{ph} \approx Gq\mu_{De}\tau_e = Gq\frac{L}{6N_D\sigma_{cross}kT}, \tag{2.9}$$

where L, N_D, σ_{cross}, are the scattering mean free path of the carriers, the defect density, and the trapping cross-section, respectively. As can be seen, photoconductivity is predicted to be proportional to the excitation intensity, G, and inversely proportional to the defect density, N_D, and to the temperature, T. Note that the capture cross-section is approximately constant and that the photoconductivity is

proportional to the illumination flux.

2.6 Summary

In this chapter, the basic characteristics of hydrogenated amorphous silicon (a-Si:H) have been reviewed. a-Si:H possesses the short range order of crystalline silicon (c-Si), but lacks its long range order. This lack of order translates into a broadening of the band edges in the density of states. Dangling bonds in a-Si:H translate into defect states in the forbidden gap as well as poorer electrical properties. Hydrogenation of the amorphous material can improve its electrical properties by passivating such dangling bonds. Electrical conduction in a-Si:H can occur either by extended state, defect state, or localized state conduction. Usually, extended state conduction dominates at high temperatures. The conduction of a-Si:H can also be changed by exposing the material to illumination. Carriers are excited from non-conducting states to conducting ones, and thus increasing conduction. Photoconductivity is proportional to the incoming illumination flux, and inversely proportional to defect density and temperature.

Chapter 3

Physics of a-Si:H n-i-p Photodiodes

The study of a-Si:H photodiodes, in particular n-i-p , started in the 1970s, when amorphous materials were first examined for their power conversion capabilities for use in solar cells [46]. Photodiodes are favored as photosensors thanks in part to their excellent performance and simple structure. MIS (Metal-Insulator Semiconductor), Schottky and n-i-p photodiodes are the three main types of hydrogenated amorphous silicon (a-Si:H) based photodiodes[47].

Hydrogenated amorphous silicon n-i-p diodes have high internal quantum efficiency, low reverse bias leakage current and can be conveniently produced on substrates such as glass or plastics. These advantages make a-Si:H n-i-p diodes practical light detectors for image sensor arrays [1]. However, a-Si:H n-i-p diodes have the drawback of lacking the photoconductive gain found in Schottky and MIS photodiodes. Although avalanche gain is observed in amorphous selenium, this is not found in a-Si:H [48].

The aim of this chapter is to summarize the essential background related to the a-Si:H n-i-p photodiode and build on the concepts presented in Chapter 2. First, the basic mode of operation of the diode is described. Then, the capacitance encountered in the device is explained. Following this, the quantum efficiency related to the photodiode operation is presented. Finally, some comments related to the noise performance are summarized.

3.1 Photodiode Device Structure

A standard n-i-p photodiode structure is shown in Figure 3.1. The design consists of two very thin p-doped and n-doped layers with a thicker undoped intrinsic layer sandwiched in-between, from which the name n-i-p is derived. The n-i-p diode also includes top and bottom metal contacts, since the doped layers have low conductivity. For example, a 10 nm thick n-type layer offers at best 10^8 $\Omega/\square$. Indium Tin Oxide (ITO) is a common transparent conductor used as the top electrode for top illumination diode structures [4]. Section 5.1.2 will describe the photodiode structure used for the experiments in further detail.

High doping in a-Si:H results in a high density of charged dangling bond defects, which in turn give rise to short minority carrier lifetimes [1]. Thus, most minority carriers generated by incident illumination recombine rapidly before they can cross the bias junction. In other words, the highly doped p and n layers do not contribute to the light sensitivity of the diode. As a matter of fact, the doped layers reduce the diode sensitivities for short wavelength illumination. On the other hand, the undoped layer is an efficient collector for the electron-hole pairs generated by incoming illumination due to its low defect density [4].

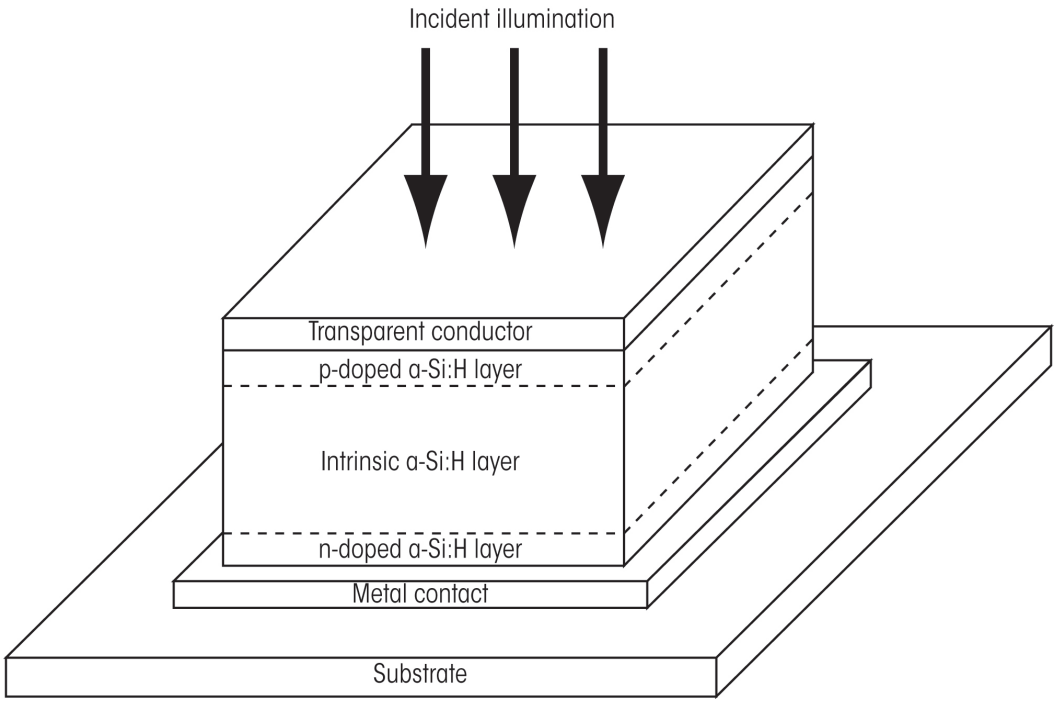

Figure 3.1: a-Si:H n-i-p diode structure [4].

3.2 Mode of Operation

The n-i-p diode has the electrical characteristics shown in Figure 3.2. The exponentially increasing forward bias current and the low reverse bias current are both similar to that of a normal p-n diode. Chapter 4 will cover further details of the current voltage characteristics. The reverse bias current increases by over four orders of magnitude under illumination. This leads to the concept that under reverse bias, the n-i-p diode can serve as a light detector. The signal from a photodiode is usually acquired by taking the difference between the photocurrent and the dark current.

The internal built-in potential, V_{bi}, gives rise to an internal electrical field.

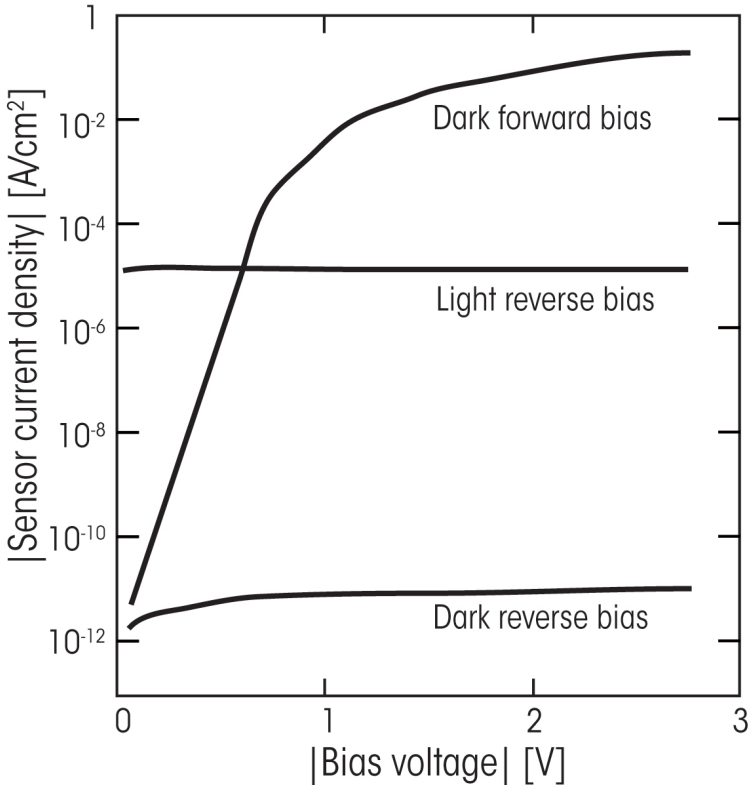

Figure 3.2: Typical electrical characteristics of a photodiode [1].

Under reverse bias, the internal electrical field is increased further. When the n-i-p diode is exposed to light, electron-hole pairs are generated in the intrinsic layer (i-layer). The generated charges are then swept by the electrical field and a current will flow. This current is termed the photocurrent, I_{ph} and can be described as follow:

$$I_{ph} = G_L \eta_{QE}(V_{bias}, \lambda), \tag{3.1}$$

where G_L, $\eta_{QE}(V_{bias}, \lambda)$ are the luminous flux and the quantum efficiency respectively. The quantum efficiency depends on the generation of electron-hole pair and the charge collection efficiency. The generation depends on the wavelength of the

incident light. Note that this is the primary photocurrent referred to in Section 2.5.

The collection efficiency depends on the bias voltage and the carrier recombination lifetimes. Defects in a-Si:H limit the carrier lifetime, τ. The carrier lifetime with free mean path, L, drift mobility, μ, and electric field, $\overrightarrow{E}$, can be expressed as:

$$\tau = \frac{L}{\mu \overrightarrow{E}}. \tag{3.2}$$

A smaller τ translates to a higher trapping probability and hence a lower collection efficiency. In order to increase the collection efficiency, a large value of $\mu\tau$ and a high applied bias are preferred.

The fraction of charge that is collected, P, is given by the Hecht formula [49]:

$$P = \frac{\mu\tau \overrightarrow{E}}{t_F} \left[1 - e^{\frac{-t_F}{\mu\tau \overrightarrow{E}}} \right], \tag{3.3}$$

where t_F is the thickness of the device. For large values of $\mu\tau$ Equation 3.3 can be approximated as:

$$P \approx 1 - \frac{t_F}{2\mu\tau \overrightarrow{E}}. \tag{3.4}$$

The value for $\mu\tau$ is different for electrons and holes. For example, in low defect density a-Si:H, $\mu\tau_{electron} = 3 \times 10^{-7}$ cm^{2}V^{-1} and $\mu\tau_{holes} = 5 \times 10^{-8}$ cm^{2}V^{-1}. The value $\mu\tau$ is inversely proportional to the density of traps, N_D and the capture cross-section, σ_{cross} and can be expressed as:

$$\mu\tau = \frac{const}{\sigma_{cross} N_D}. \tag{3.5}$$

Neutral dangling bonds in undoped a-Si:H can trap both electrons and holes. In other words, N_D is the same for both kinds of carriers. However, the cross section

for holes is greater, so the $\mu\tau$ for holes is smaller than that for electrons [1].

3.3 Defects and Metastability

By taking the difference of the signal of an image in darkness and an image taken under illumination, one can eliminate any unwanted offset or dark current and obtain the image desired. If the dark current characteristics of the photodiode are constant, then a one-time calibration of the photodiode will be sufficient. On the other hand, if the behavior of the diode changes over time, then frequent measurements need to be made. Note that if the dark current is very low, then the effects of an unstable current is not as significant, making low leakage current devices very desirable. Schottky diodes tend to have higher leakage currents than n-i-p photodiodes at room temperatures [4]. Schottky diodes also have higher leakage currents than n-i-p detectors at lower biases [4].

The quality of the a-Si:H can decay over time under prolonged illumination due to the metastable nature of the material (see Section 2.3) [42]. The Staebler-Wronski effect can therefore cause a reversible change in the current characteristics of the device [42]. However, the exposure of photodiodes under normal conditions is much less than the magnitude required to create defects. In other words, the Staebler-Wronski effect is not practically important in n-i-p diodes under typical duty cycle and exposure conditions. This is because the exposure dose and time are not enough to cause a significant increase in the defect density of the intrinsic layer. Note that this does not mean that the Staebler-Wronski does not happen in n-i-p photodiodes, photodegradation of the leakage current is observed with the proper light exposure [50].

Other possible causes for current fluctuations in the photodiode are related to the conduction mechanism found in the photodiode. For example, transient behavior is observed in reverse bias current after the application of bias and several seconds are required before stable operation can resume [50]. Another possible source of current instability comes from the fact that the leakage current is temperature dependent. Section 4.1 examines the temperature dependence of the reverse bias current. In addition, the photodiode current fluctuates with bias, since the leakage current changes over time. Since the photodiode is operated under integration mode, every time a photon strikes the i-layer, carriers are generated, charge builds up at the contacts and effectively decreases the bias. Thus, the measured dark current characteristics might not accurately represent the situation for the illuminated diode.

3.4 Capacitance

The response speed of a general photodetector is dependent on three factors: diffusion of carriers, drift time in the depletion region and capacitance of the depletion region [51]. The first factor states that carriers generated outside the depletion region must diffuse to the junction which results in considerable time delay. However, in a-Si:H n-i-p diodes, there are no free carriers outside the depletion region. Thus, for a-Si:H n-i-p photodiodes, the first factor does not apply [1]. The second factor, the drift velocity in the depletion region, is determined by the bias. With sufficient reverse bias, the drift velocity will reach saturation. However, there are also some limitations related to the reverse bias due to the bias dependence of the dark current. Finally, the depletion region capacitance also affects the response

speed in two ways. If the depletion region is too large, the transit-time effects will limit the frequency response. On the other hand, a thin depletion layer results in a larger capacitance value (C), which results in a high RC time constant, where R is the load resistance.

As mentioned above, the capacitance of the n-i-p diode is critical since it determines the response time of the circuit. The diode's capacitance can be subdivided into three sections: (i) the p-i junction capacitance, (ii) the i-layer capacitance and (iii) the n-i capacitance. Hegedus assumes that the n-i junction forms an ohmic contact whose space charge region is very narrow. In other words, the n-i capacitance is large when compared to the other capacitances and can be neglected when connected in series [5]. Shown in Figure 3.3 is the band diagram used to derive the equivalent capacitance of a n-i-p diode. The junction shown in Figure 3.3 has no applied bias. The states below the Fermi energy are assumed to be filled. Before describing the equations related to the junction capacitance, the variables in Figure 3.3 need to be defined. The variables E_C, E_F, E_V are the conduction band energy, the Fermi energy and the valence band energy levels respectively. The variable V_B is the barrier height and d is the thickness of the i-layer. The variable V_D is the diffusion potential and is given by:

$$V_D = \frac{qV_B - E_F}{q}. \tag{3.6}$$

E_E is defined as the cut-off energy dividing the intrinsic layer into a responsive ($x < X_E$) and unresponsive state ($0 < x < X_E$). The responsive state is often referred to as the conductive region and the unresponsive state to the space-charge region. This separation of the i-layer can be explained by the thermal emission of electrons from a gap state, only states which can release their charge within the

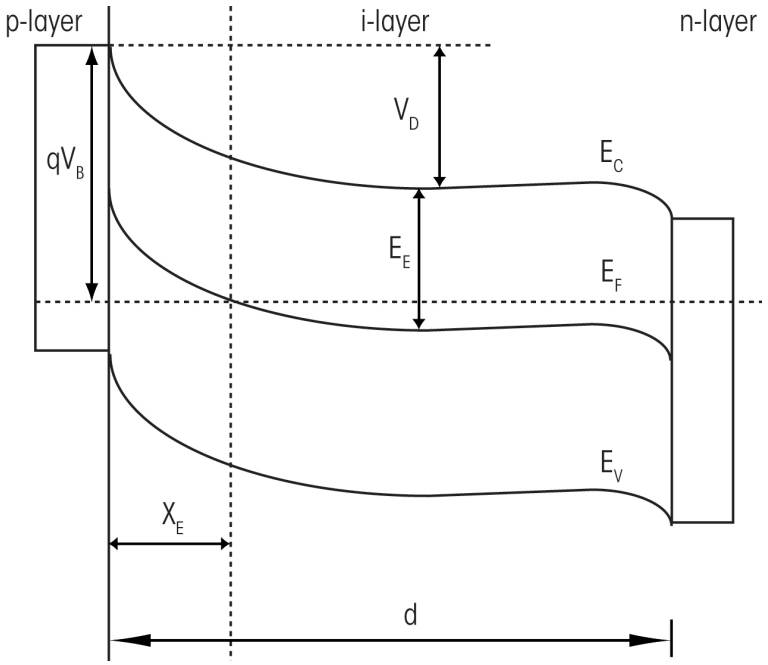

Figure 3.3: a-Si:H n-i-p diode band diagram used to describe the capacitance. [5]

a.c. period will be able to follow the a.c. signal. The thermal emission time of an electron, τ_E, from a gap state at a distance E below the conduction band $E_C(x)$ is described as:

$$\tau_E = \upsilon^{-1} e^{-\frac{E}{kT}}, \tag{3.7}$$

where ν is the attempt-to-escape frequency. The variable E_E is defined as:

$$E_E = kT \ln\left(\frac{\upsilon}{\omega}\right), \tag{3.8}$$

where ω is the frequency of the applied a.c. bias signal.

By using Poisson's equation and assuming a uniform distribution of mid-gap

states, $g(E_F) = g_0$, the following equations are derived:

$$\begin{aligned} V(x) &= V_D e^{-\frac{x}{L_0}}, \\ \overrightarrow{E}(x) &= -\frac{V_D}{L_0} e^{-\frac{x}{L_0}}, \\ \rho(x) &= -\frac{V_D}{L_0^2} e^{-\frac{x}{L_0}}, \end{aligned} \tag{3.9}$$

where $V(x)$, $\overrightarrow{E}(x)$, $\rho(x)$ are the electric potential, electric field and space charge profile respectively. The value L_0 is defined as the screening length and is given by:

$$L_0 = \sqrt{\frac{\varepsilon}{q^2 g_0}}. \tag{3.10}$$

The boundary conditions used by Hegedus assume that the electric potential and electric field are zero at $x = \infty$ [5]. Note that in real n-i-p devices with finite thickness d, this is not strictly true. However, if $d > 3L_0$ then this approximation holds and simplifies the calculations greatly.

The capacitance in the conductive region ($x > X_E$) is quasi-static, since all the charges in the deep state can respond, this gives rise to the following d.c. value capacitance:

$$C_{DC} = \frac{\varepsilon}{L_0}, \tag{3.11}$$

since L_0 is the first moment of the charge distribution. By using Equation 3.10, Equation 3.11 can be re-written as:

$$C_{DC} = \sqrt{\varepsilon q^2 g_0}. \tag{3.12}$$

The capacitance of the unresponsive region ($0 < x < X_E$) in turn is described

by:

$$C_{XE} = \frac{\varepsilon}{X_E}. \tag{3.13}$$

Hence, the junction capacitance, C_J, for an arbitrary a.c. period is described by the series capacitance of C_{DC} and C_{X_E}, which is:

$$C_J = \frac{\varepsilon}{X_E + L_0}. \tag{3.14}$$

The bulk capacitance on the other hand is:

$$C_B = \frac{\varepsilon}{(d - X_E)}. \tag{3.15}$$

Finally, the total capacitance of the photodiode is the series capacitance of the junction and bulk capacitance and is given by:

$$C_{Total} = \frac{\varepsilon}{(d + L_0)}. \tag{3.16}$$

3.5 Quantum Efficiency

Quantum efficiency, η_{QE}, is defined for photodiodes as the number of electron-hole pairs generated per incident photon:

$$\eta_{QE} = \left(\frac{I_{ph}}{q}\right) \Big/ \left(\frac{P_{opt}}{h\upsilon}\right), \tag{3.17}$$

where I_{ph}, q, P_{opt}, h, and υ are the photogenerated current, the elementary charge, the optical power at wavelength λ, the plank constant, and the frequency of the incident photon respectively. Quantum efficiency (QE) is usually expressed as a

percentage [51].

A related figure of merit is responsivity, R. Responsivity is defined as the ratio of the photocurrent in Amperes to the optical power incident to the photodiode in Watts. Responsivity is used to measure the sensitivity of a photodiode. The higher the responsivity, the more sensitive the diode is, and the more current it can generate. The responsivity can be related to the quantum efficiency, described in Equation 3.17, as follows:

$$R = \frac{I_{ph}}{P_{opt}} = \frac{q\eta_{QE}}{h\upsilon} = \frac{\lambda\eta_{QE}}{1.24}, \tag{3.18}$$

where wavelength λ is expressed in μm [51]. As mentioned previously, for a-Si:H n-i-p diodes, a QE of 100 % is unattainable. However, it has been shown that an optimized designed can achieve a quantum efficiency of $\sim 80 - 90$ % at wavelengths between 500 to 600 nm [1].

Note that the responsivity and η_{QE} both depend on the wavelength of the incoming radiation. Therefore, the spectral response of a photodiode, which shows the sensitivity of the diode to the photons at different wavelengths, is an important parameter. The spectral response of the photodiodes can be improved by the application of a surface coating. By varying the material coating, the spectral response can improve the response of targeted wavelengths up to 25 % and reduce the spectral response at other frequencies.

3.6 Noise

Noise is described as the unwanted signal that degrades the signal of interest. Random events at the microscopic level translate into macroscopic fluctuations of current, voltage and charge. Unfortunately, electronic noise is omnipresent in all circuits and devices, any object capable of allowing the flow of electrical current will exhibit noise. Hence, a good understanding of noise is necessary.

Since noise is random, it is studied by statistical means and usually has a mean value of zero. The effective noise power of a source is measured in root mean square (RMS) values. If the RMS values of different random noise sources are uncorrelated, they can be added together as:

$$x^2 = \sum_i x_i^2, \tag{3.19}$$

where x_i are the RMS values of the individual noise sources [4].

3.6.1 Different Noise Sources

There are various sources of noise and they are each caused by different electrical components. In electronic circuits, resistance generates thermal noise, also refereed to as Johnson-Nyquist Noise. Current sources cause shot noise. Semiconductor devices contribute flicker noise and generation-recombination noise [4].

Johnson-Nyquist Noise

The Johnson-Nyquist noise is the random variation in current and voltage caused by the Brownian movement of electrons in a resistive medium. This type of noise

was first measured and described by John B. Johnson at Bell Labs in 1928 [52] and explained by Harry Nyquist [53]. Thermal noise was first observed in resistors, but can be applied to any type of conducting medium. It can be modeled by a voltage source in series with a noise generating resistor or a shunt current generator. Thermal noise has a flat power spectrum and is known as white noise. The power spectral density of the generator can be expressed as:

$$\overline{v}^2_{n_{Thermal}} = 4kTR, \tag{3.20}$$

where k is Boltzmann's constant, T is the temperature of the resistor and R is its value. Hence, for a given bandwidth, the RMS fluctuation of the voltage is:

$$v_{n_{Thermal}} = \overline{v}_{n_{Thermal}}\sqrt{\Delta f} = \sqrt{4kTR\Delta f}, \tag{3.21}$$

where Δf is the bandwidth over which the noise is measured. Note that thermal noise is directly proportional to temperature; as temperature decreases, so does thermal noise.

In the literature, there is often reference to another noise source called kT/C noise. kT/C noise is not a fundamental noise source, but rather thermal noise in another guise. Consider for example a low-pass filter composed of a resistor and a capacitor, with the output voltage measured across the capacitor. The noise bandwidth, Δf, expressed in Hertz is:

$$\Delta f = \frac{1}{2\pi}\int_0^\infty \frac{d\omega}{1+(\omega RC)^2} = \frac{1}{4RC}, \tag{3.22}$$

where ω, R, C are the frequency, the resistor value and the capacitor value, respectively. Using Equation 3.21, the total output noise voltage measured across the

capacitor is:

$$v_{n_{KTC}} = \overline{v}_{n_{Thermal}}\sqrt{\Delta f} = \sqrt{\frac{4kTR}{4RC}} = \sqrt{\frac{kT}{C}}. \tag{3.23}$$

As can be seen, this is not a new source, but thermal noise in the presence of a filtering capacitor. Therefore, thermal noise and kT/C should not be included in the same single noise calculation [54].

Shot Noise

Shot noise arises from the fact that an apparently constant current is actually composed of random independent movements of a large number of charge carriers. Shot noise is generally observed in p-n junctions, as current flows across it and it is dependent on bias current and the electron charge. In a diode, electrons are randomly ejected from the n-region and, if they have enough energy, they will overcome the potential barrier at the junction and enter the p-region. However, electrons might also collide with lattice vibrations, surface state, or impurities and fall back into the n-region. Even if the electrons do make it through the barrier, there still exists a number of randomizing conditions on the other side. Eventually, the electron will travel all the way to the metal contact. Each arrival of such an electron at the drain contributes an impulse of charge. The impulse of charge in the time domain translates to wideband noise in the frequency domain that becomes larger with increasing average current. Shot noise occurs not only in p-n junctions but also in any conductor, and even in the case where the charge is not well localized. Although shot noise is due to a completely different mechanism from thermal noise, they are both quantum fluctuations and some researchers treat them as a single unified concept [55].

Shot noise can be modeled as a Poisson process and the charge carriers which make up the current will follow a Poisson distribution. The resulting current has standard deviation of:

$$\sigma_{n_{Shot}} = \sqrt{2qI\Delta f}, \tag{3.24}$$

where q, I, and Δf are respectively the elementary charge, the average current through the device, and the bandwidth over which the noise is measured.

Flicker Noise

Flicker noise was also discovered by Johnson at Bell Labs in 1925 [56]. Flicker noise has a "pink" spectrum, where its power spectral density is inversely proportional to the frequency (f) [57]. The spectrum varies as $1/f^{\alpha}$, where the exponent is approximately unity ($\alpha = 1 \pm 0.2$). Flicker noise is therefore often referred to as 1/f noise. 1/f noise is present in most electronic devices at low frequencies and can be expressed as:

$$i_{n_{Flicker}} = \sqrt{\bar{i}^{2}_{n_{Flicker}}} = \sqrt{k\Delta f \frac{I^a}{f^b}}, \tag{3.25}$$

where k, I, a, f, b, Δf are the proportionality constant, the average direct-current (DC) current, the current fitting parameter, the frequency, the frequency fitting parameter, and the bandwidth over which the noise is measured respectively [57]. The current fitting parameter, a, varies between 1.5 and 2. The frequency fitting parameter, b, varies within 0.8 and 1.4. The proportionality constant, k, depends on the device process. Flicker noise is usually defined by a frequency called the corner frequency (f_c), which is the frequency at which the extended inverse frequency line crosses the unity noise temperature ratio. In other words, the "white" thermal noise dominates for frequency above f_c.

There are two competing theories that are used to explain the origin of flicker noise: the McWhorter number fluctuation [58] and the Hooge mobility fluctuation theory [59]. Since there are experimental results to support both theories, researchers do not have conclusive evidence to favor one over the other.

McWhorter, who worked on germanium filaments, proposed that flicker noise is a surface effect. He attributed the source of 1/f noise to a fluctuation in the majority carrier density near the semiconductor surface due to a fluctuation of surface interface traps. He showed in a number of experiments that the flicker noise in germanium depends on the ambient atmosphere of the filament. McWhorter derived the 1/f noise spectrum by assuming that the time constant τ of the surface states varied with a $1/\tau$ distribution. However, the number fluctuation theory fails to account for the flicker noise in ionic solutions, which does not have interface traps.

Hooge, who worked on metal films [60], proposed that flicker noise is a bulk phenomenon [59]. From his experiments, Hooge proposed the empirical relation of flicker noise in terms of resistance fluctuation as:

$$R^2_{n_{Flicker}} = \frac{\alpha_H}{N}\frac{R^2}{f}, \tag{3.26}$$

where $R^2_{n_{Flicker}}$ is the spectral density of the resistance, N is the total number of free carriers in the bulk, α_H is the Hooge constant, R is the resistance, and f is the frequency. The variable α_H is a dimensionless empirical parameter with a value $\sim 2 \times 10^{-3}$. The Hooge constant does not hold for all media and needs to be modified depending on the impurity scattering in the material [61].

Generation-Recombination Noise

Trapping and de-trapping centers in the bulk can cause generation-recombination (G-R) noise. The trapping and de-trapping mechanisms change the total number of carriers, hence the current, and thus causes a fluctuation in the resistance. The spectral density of the resistance fluctuation can be expressed as:

$$R^2_{n_{G-R}} = \frac{\sigma^2_{G-R}}{N^2} \frac{4\tau R}{1+\omega^2\tau^2}, \tag{3.27}$$

where σ^2_{G-R}, N, τ, ω, R are the variance, the total number of free carriers in the bulk, the trap relaxation time, the angular frequency, and the resistance respectively [62]. The variance can be expressed as:

$$\frac{1}{\sigma^2_{G-R}} = \frac{1}{N} + \frac{1}{N_{Occupied}} + \frac{1}{N_{Empty}}, \tag{3.28}$$

where N, $N_{Occupied}$, N_{Empty} are the total number of free carriers in the bulk, the number of occupied traps, and the number of empty traps respectively.

3.6.2 Noise in a-Si:H photodiodes

Noise in a-Si:H photodiodes have been studied extensively for different device configurations[63] [64] [65]. In general, two noise sources are considered: flicker and thermal noise [65]. Researchers report that the current dependent flicker noise is the main noise source at high biasing condition. For low bias conditions, the bias independent Johnson-Nyquist Noise dominates [66].

Flicker Noise in a-Si:H photodiodes

Noise behavior in a-Si:H photodiodes was found to follow flicker noise characteristics of approximately 1/f or $1/f^2$. This has been attributed to the trapping and de-trapping of electrons by distributed trapping centers in the band gap or to inhomogeneous current filaments [63] [67]. However, Wieczorek showed that none of the following models could explain the observed empirical results (Hooge's model (see Section 3.6.1), the recombination model, the bulk trapping model, the surface trapping model, and the bulk conductance fluctuation model). Instead, Wieczorek proposes that flicker noise results from the injection of carriers from the doped contact regions into the diode bulk. Wieczorek also showed experimentally that flicker noise is independent of the deposition order and that flicker noise power scales with the diode area. [66]

Thermal Noise in a-Si:H photodiodes

As described in Section 3.6.1, series resistance causes thermal noise. In a-Si:H p-i-n or n-i-p photodiodes, the series resistance arises from the resistances of the semiconductor layers, the metal contacts, and the metal-semiconductor interfaces. Since the valence band-tails are wider than those in the conduction band, the resistance of p-type a-Si:H is much larger than that of n-type a-Si:H. The resistance of the p-layer can be estimated as:

$$R_{p-layer} \approx \frac{d_p}{A\sigma_0 e^{-\frac{\Delta E_p}{kT}}}, \tag{3.29}$$

where d_p, A, σ_0,ΔE_p, k, T are the p-layer thickness, area of the diode, conductivity prefactor, and the p-type activation energy respectively [68].

3.7 Summary

This chapter introduced some of the theoretical equations related to the physical operations of a a-Si:H n-i-p photodiode. The n-i-p structure requires the use of an intrinsic layer for photocurrent generation, since the doped layers are high in defect density and unsuitable for photodetection. Incoming photons generate electron hole pairs in the i-layer that then migrate to the terminals giving rise to the photocurrent. Since the signal of interest is obtained by subtracting the photocurrent from the dark current, current stability is a primary concern. The Staebler-Wronski effect does not apply to n-i-p photodiodes, but other possible causes of current fluctuations are related to the conduction mechanism. The capacitance of the photodiode is also important, since it determines both the response speed and the storage capacity of the photodiode. The quantum efficiency defines the quantity of charge generated for the incoming photons. Finally, noise in the photodiode can obscure the signal of interest and needs to be studied as well. Possible noise sources in photodiodes include flicker and thermal noise.

Chapter 4

Modeling of a-Si:H n-i-p Photodiode

A complete theoretical model of a n-i-p photodiode requires the simultaneous solution of a complete set of transport equations [23]. The set of equations includes the electron and hole continuity equations:

$$-\frac{1}{q}\frac{dJ_n}{dx} = G(x) - R(x), \tag{4.1}$$

$$\frac{1}{q}\frac{dJ_h}{dx} = G(x) - R(x), \tag{4.2}$$

and the Poisson's equation:

$$\frac{d\overrightarrow{E}}{dx} = \frac{\rho(x)}{\varepsilon}, \tag{4.3}$$

where G is the generation rate and R is the recombination rate. $\overrightarrow{E}$ is the electric field and ρ is the space-charge density.The values J_n, J_p are the electron and hole

conduction current densities and can be expressed as:

$$\begin{aligned} J_n &= q\mu_n \left(n\overrightarrow{E} + \tfrac{kT}{q}\tfrac{dn}{dx} \right), \\ J_h &= q\mu_h \left(h\overrightarrow{E} + \tfrac{kT}{q}\tfrac{dh}{dx} \right) \end{aligned} \tag{4.4}$$

where μ_n, μ_h are the band mobilities of the electrons and holes, T is the temperature, and ε is the dielectric constant of a-Si:H. To determine the space-charge density, the electron concentration (n), the hole concentrations (h), and the distribution of localized states need to be considered. As can be seen, a theoretical model for a n-i-p diode is quite complex and requires knowledge of the distribution of density of states in the mid-gap. Although a theoretical model offers a greater insight about the physical behavior of the device, it is time-consuming to simulate. An empirical model is therefore suggested as an alternative way to simulate the photodiode.

The previous chapters have covered the essential building blocks from which the a-Si:H photodiode model will be built. Starting from the ideal equations, an empirical model will be derived. This chapter will explore the different components that are part of the a-Si:H photodiode. Shown in Figure 4.1 is a simplified equivalent model of the a-Si:H photodiode. The model is composed of a resistor, a diode, a capacitor and a current source. The resistor represents the series resistance found in the photodiode. The diode summarizes the current characteristics. The capacitor is used to express the photodiode capacitance and the current source to emulate the photocurrent generated by the photodiode under illumination.

First, the current-voltage characteristics, including forward and reverse bias, will be examined in Section 4.1. This section will also briefly describe the series resistance. Then, a model for the capacitance of the photodiode will be presented

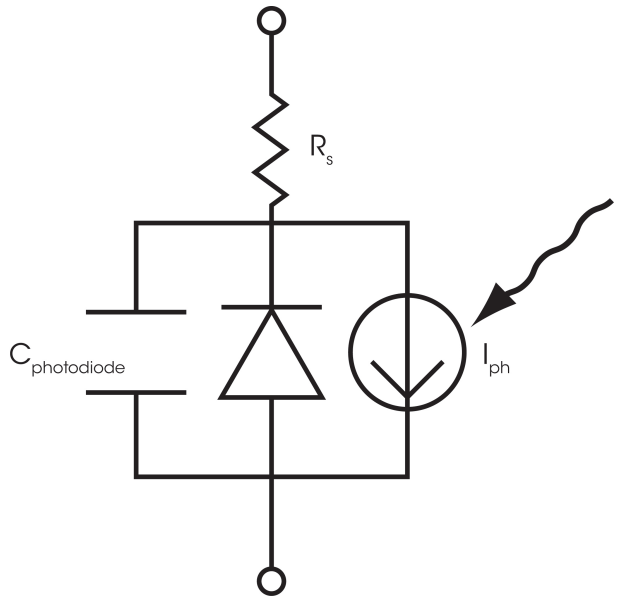

Figure 4.1: Equivalent circuit model for a a-Si:H photodiode.

in Section 4.2. Finally, the model for the photocurrent of the photodetector is explained in Section 4.3.

4.1 Current-Voltage Characteristics

Section 3.2 introduced the basic mode of operation of the photodiode. As previously described, the current generated by the photodiode is used to quantify the strength of the incoming signal. Hence, the current-voltage (I-V) or current density-voltage (J-V) characteristics and its model are at the core of the model. The forward bias and reverse bias current characteristics are modeled separately. They are presented in Subsection 4.1.1 and Subsection 4.1.2 respectively.

4.1.1 Forward Bias Photodiode Current

The n-i-p diode is rarely operated in the forward bias mode for photodetection. However, the forward bias region is very useful in determining the defect density of the i-layer. For this reason, this model will also examine the forward bias characteristics associated with the n-i-p diode. Figure 4.2 illustrates the forward bias characteristics of a-Si:H n-i-p photodiodes fabricated at the Giga2Nano Laboratory.

The forward bias current behaves diode-like, namely its current increases exponentially with the bias. The forward bias current can be described ideally by the equation:

$$I_F(V_{bias}) = I_0(e^{\frac{qV_{bias}}{nkT}} - 1), \tag{4.5}$$

where I_0, q, V_{bias}, n, k, T are the saturation current, elementary charge, bias potential, ideality factor, Boltzmann's constant, and temperature respectively.

In Equation 4.5, n varies empirically from 1.3 to 1.5 [51]. The ideality factor depends on the thickness, the deposition conditions and the quality of the contacts. Theoretically, the ideality factor is 1 for thermionic emission. On the other hand, the ideality factor is 2 for a generation-recombination mechanism. The contribution of both components depends on the barrier height and the density of recombination states. The thermionic emission current is inversely proportional to the barrier height. The generation-recombination mechanism is proportional to the number of recombination states. Recall that in a-Si:H the recombination centers are usually the defects situated in the mid-gap. Studies show that the high barrier from the p-type contact is enough to suppress thermionic emission [69]. Although, the measured ideality factor is greater than 1, modeling shows that the main contribution

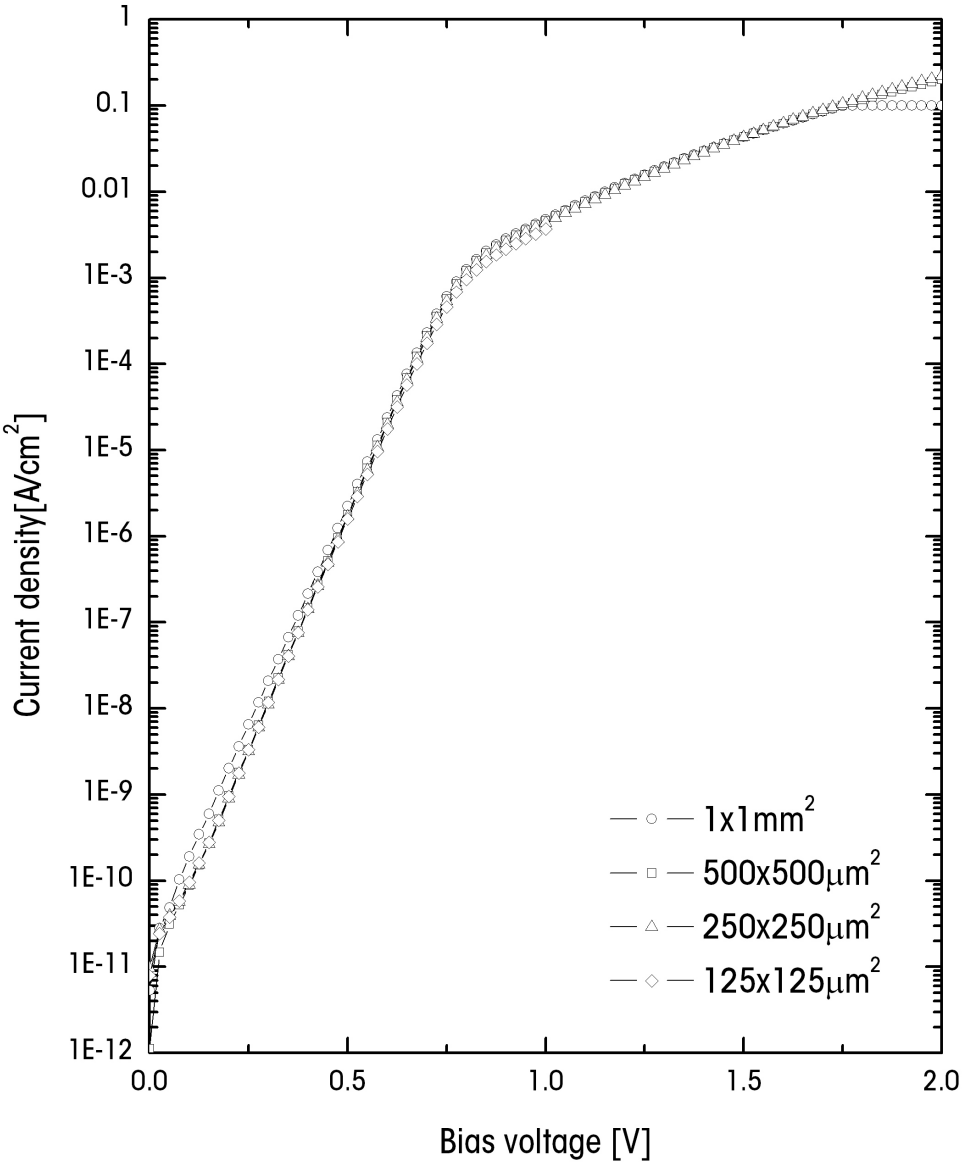

Figure 4.2: Forward bias J-V characteristics of a-Si:H photodiodes at 40 °C.

still comes from the generation-recombination mechanism. This is also consistent with the statement that the main contribution for reverse bias current comes from thermal bulk generation.

As seen in Figure 4.2, the current deviates from the exponential relationship at higher bias. This can be explained by the fact that the current increases exponentially until there is a series-resistance or recombination limitation [50]. The series resistance can originate either from the bulk or the contacts. The contacts are usually thin films with significant resistance. As for the bulk component, a defective or thick device can create a high resistance as well. The recombination limitation becomes apparent when the trapped space-charge density exceeds the free-carrier density by orders of magnitudes [70].

A possible model for the deviation from the ideal diode equation is to use a bias dependent diode ideality factor. However, this method also requires the density of states of the i-layer, which is usually hard to obtain [71]. Another method, which is the one being presented here, is to separate the forward bias I-V model into three regions: (i) low, (ii) medium and (iii) high biases. Three different equations are then used to describe the quasi-static voltage characteristics of these three regions.

The low forward bias region follows the ideal diode equation, Equation 4.5. Equation 4.5 can be expressed in terms of current density, $J_{F_{low}}$, as :

$$\begin{aligned} I_F(V_{bias}) &= A \times J_{F_{low}}(V_{bias}), \\ J_{F_{low}}(V_{bias}) &= J_{0_{low}}(e^{\frac{qV_{bias}}{nkT}} - 1), \end{aligned} \tag{4.6}$$

where A , $J_{0_{low}}$ are the junction area and saturation current density of the photodiode respectively. The variables $J_{0_{low}}$ and n are both temperature dependent and

can be expressed as [51]:

$$\begin{aligned} J_{0_{low}}(T) &= A_{0_{low}} \mathrm{e}^{\left(-\frac{E_{a_{low}}}{kT}\right)}, \\ n(T) &= n_0 - \delta_n T, \end{aligned} \tag{4.7}$$

where $A_{0_{low}}$ is the pre-exponential factor dependent on the processing conditions, $E_{a_{low}}$ is the forward bias activation energy, n_0 is the ideality factor at 0 K, and δ_n is the reduction constant of the ideality factor.

For medium forward biases, the series contact resistance, R_s, reduces the voltage across the photodiode. The current density is reduced by a factor of:

$$\exp\left(\frac{qIR_s}{nkTA}\right) = \exp\left(\frac{qIR_\square}{nkT}\right), \tag{4.8}$$

where $R_\square$ is the sheet resistance and can be expressed as $R_\square = R_s/A$. The above equation can be explained by the schematic shown in Figure 4.1. The series resistance, R_s, reduces the potential that the diode sees. By using Kirchhoff's voltage law (KVL), Equation 4.5 becomes:

$$I_F(V_{bias}) = I_0 \left(e^{\frac{q\left(V_{bias} - I_F R_s\right)}{nkT}} - 1\right) \tag{4.9}$$

Since the series resistance tends to be very small, it can usually be ignored for the photodiode model.

For the high bias region, the current-voltage follows a power law relationship due to space-charge limited current. The current-voltage relationship can be expressed as:

$$J_{F_{high}}(V_{bias}) = J_{0_{high}} V_{bias}^{\gamma}, \tag{4.10}$$

where $J_{0_{high}}$, and γ are the high bias saturation current, and the high bias region exponent respectively. The variables $J_{0_{high}}$ and γ are also temperature dependent and can be modeled as:

$$\begin{aligned} J_{0_{high}}(T) &= A_{0_{high}} \mathrm{e}^{\left(-\frac{Ea_{high}}{kT}\right)}, \\ \gamma(T) &= \gamma_0 - \delta_\gamma T, \end{aligned} \tag{4.11}$$

where $A_{0_{high}}$, $E_{a_{high}}$, k, T, γ_0, and δ_γ are the exponential pre-factor, the activation energy, the Boltzmann's constant, the temperature, the exponential at 0 K, and the change of the exponential temperature correctional factor respectively.

A weighting function can be used to combine both curves and to smooth out the transition between the low and high bias regions of the graph. For the model, the weighting function was chosen to be:

$$f_{weight}\left(V_{bias}\right) = \frac{1}{1 + e^{[f_p(V_{bias} - f_q)]}}, \tag{4.12}$$

where f_p is the scaling parameter and f_q is the center parameter. The weighting function is loosely based on the Fermi-Dirac distribution function. The smoothing of the curves can be determined by the f_p parameter and the transition region is governed by the f_q parameter. In short, taking the above considerations, the combined equation for the forward I-V characteristics is:

$$\begin{aligned} J_F\left(V_{bias}, T\right) = & \underbrace{J_0(T) e^{\left(\frac{qV_{bias}}{n(T)kT}\right)}}_{J_{F_{low}}} \cdot \underbrace{\frac{1}{1 + e^{\left[f_{p_{low}}\left(V_{bias} - f_{q_{low}}\right)\right]}}}_{f_{weight_{low}}} \\ + & \underbrace{J_{0_{high}}(T) V_{bias}^{\gamma(T)}}_{J_{F_{high}}} \cdot \underbrace{\frac{e^{\left[f_{p_{high}}\left(V_{bias} - f_{q_{high}}\right)\right]}}{1 + e^{\left[f_{p_{high}}\left(V_{bias} - f_{q_{high}}\right)\right]}}}_{1 - f_{weight_{high}}} \end{aligned} \tag{4.13}$$

4.1.2 Reverse Bias Photodiode Current

The dark reverse bias current is often used as a measure of the electronic performance of a n-i-p photodiode. A low reverse bias current is usually associated with a good device, because the reverse bias current is subtracted from the photocurrent to obtain the image of interest. Therefore, low leakage current devices are desirable. According to the ideal diode model, the reverse bias current should be equal to the saturation current I_0. However, empirically it has been observed that this is not the case. The higher dark reverse current values are likely caused by pin-hole and microstructural shunt paths of the junction or from the junction sidewalls [72]. Figure 4.3 shows the different components found in reverse bias dark current. Bulk thermal generation, doped contact injection, and edge leakage of the exposed diode are some of the components that may contribute to the diode reverse bias dark current. This section will examine all three of these components in turn. Note that some researchers also include a corner component, which scales with the number of corners in the diode [73].

Bulk Thermal Generation

The bulk thermal component scales with the photodiode area. In an optimized diode, the bulk component is the major contributor to the dark reverse bias current. Figure 4.4 illustrates the thermal generation of electrons and holes via mid-gap defect states. Due to thermal energy, electrons are excited from the valence band to an empty or singly occupied defect state. The electrons are then further excited to the conduction band [6] [50]. Shockley-Read-Hall (SRH) statistics can be used to describe the current generation from a single trap level [51]. For multi-level and continuous distribution of traps, the generation current is dominated by the

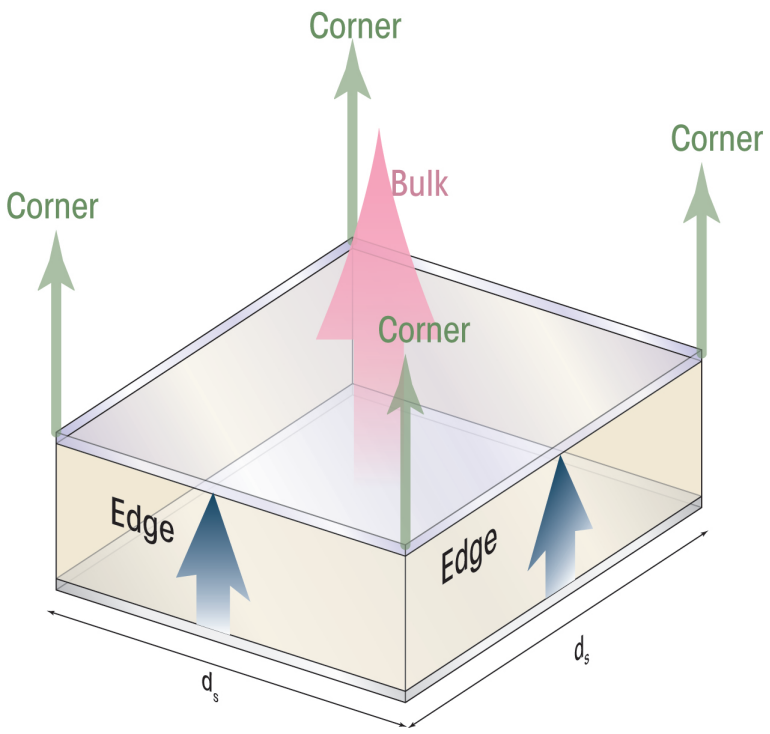

Figure 4.3: Illustration of different leakage current components found in a-Si:H photodiodes [2].

emissions from traps located within kT of the quasi-Fermi level (E_{FD}). Assuming full depletion and unity collection efficiency, the thermal generation current density, J_{th}, can be expressed by:

$$J_{th} = qN\left(E_{FD}\right) kT\omega_0 \exp\left[-\frac{q\left(E_C - E_{FD}\right)}{kT}\right] t_i, \tag{4.14}$$

where E_C is the conduction band energy level, E_{FD} is the energy defining the occupancy of localized states near mid-gap, $N_D(E_{FD})$ is the defect density in the forbidden gap, ω_0 is the excitation prefactor, and t_i is the intrinsic layer thickness [6]. The different capture cross sections for electrons and holes result in a different

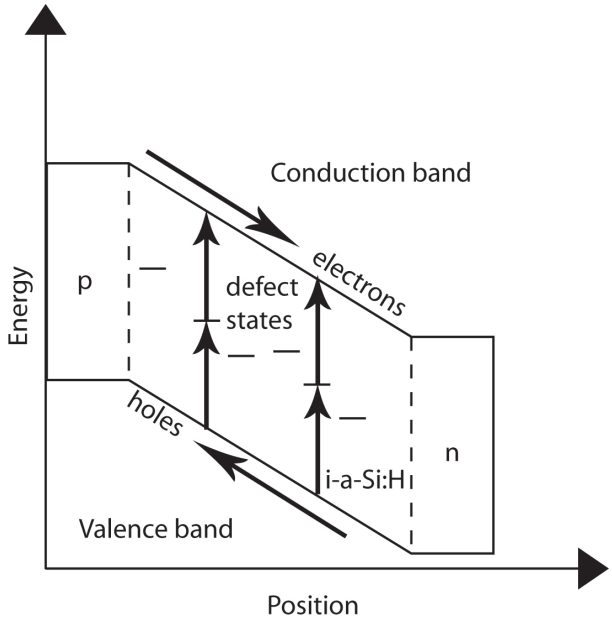

Figure 4.4: Band model illustrating bulk thermal generation [4].

rate prefactor, which shifts the quasi-Fermi energy level. The value $E_C - E_{FD}$ is approximately 0.9 eV and can be obtained from:

$$E_C - E_{FD} = \frac{1}{2}E_\mu + \frac{1}{2}\frac{kT}{q}\frac{\sigma_e}{\sigma_h}, \tag{4.15}$$

where E_μ, $\frac{\sigma_e}{\sigma_h}$ are the mobility gap and the carrier capture cross section ratio respectively. From the above equation, thermal current is temperature and defect density dependent.

$N_D(E_{FD})$ which is empirically found to be ~ 6 to 8×10^{15} cm^{-3} can be obtained from photodiode transient current experiments by measuring the depletion charge, Q_D. This is shown in Figure 4.5.

Undoped a-Si:H is naturally n-type, meaning that its equilibrium Fermi level,

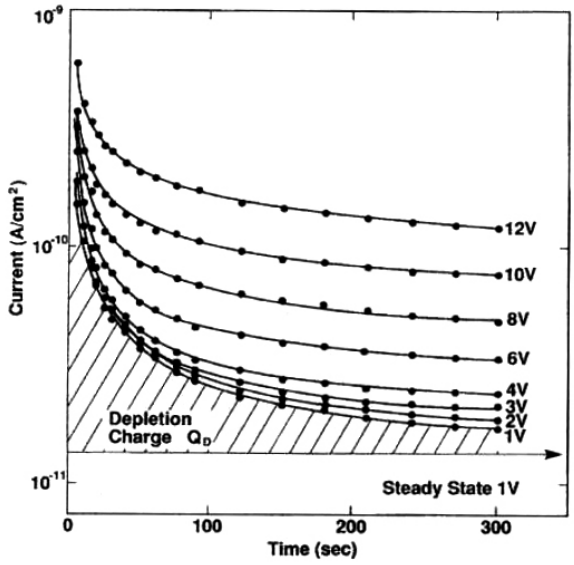

Figure 4.5: Transient reverse bias current measurements at different bias voltages for a 100×100 μm^2 diode at room temperature [6].

E_F, lies slightly above the mid-gap when there is no bias voltage. When a reverse bias is applied, a depletion of electrons is observed. The occupied states above mid-gap are depleted of charge giving rise to an initial thermal generated electron current greater than the steady state thermal current, I_{th}. Over time, the depletion continues until steady state thermal generation is reached. The initial current can be described as follows:

$$I_{th}(0) = I_{th} e^{\frac{\Delta E}{kT}}, \tag{4.16}$$

where ΔE is the position of the E_F above mid-gap.

The depletion charge released during transient measurements is caused by the shift in the Fermi level from E_F to E_{FD} after the application of the bias voltage. The depletion charge can be extracted from the measured current transient $I_d(t)$,

by integrating the area under the curve, as:

$$Q_D = \int_0^\infty I_d(t)\,dt - I_{th} \tag{4.17}$$

Another way to express Q_D is to integrate the density of states of the shaded region of Figure 4.6:

$$Q_D = q\int_{E_{FD}}^{E_F} N(E)\,dE \tag{4.18}$$

Note that unlike Figure 2.3, Figure 4.6does not differentiate between the two types of defects found in a-Si:H. By assuming that $N_D(E)$ stays constant between E_{FD} and E_F, Equation 4.18 can be approximated as:

$$Q_D = q\int_{E_{FD}}^{E_F} N_D(E)\,dE \approx qN_D(E_{FD})\,\Delta E \tag{4.19}$$

A constant $N_D(E)$ over the region of integration is a reasonable assumption since the region is well outside of the band tails. From Equation 4.19, $N_D(E_{FD})$ can be extracted as:

$$N_D(E_{FD}) \approx \frac{Q_D}{q(E_F - E_{FD})} \tag{4.20}$$

The thermal electron current decreases non-exponentially with applied voltage. The decay time constant can be described as:

$$\tau_{th} = \omega^{-1} e^{\frac{E_C - E_F(t)}{kT}} \tag{4.21}$$

Since the Fermi energy is time dependent, the decay is non-exponential. From Equations 4.16 and 4.21, one can see that both I_{th} and τ_{th} are thermally activated. This implies that a change in temperature can seriously affect the leakage current. This is confirmed by the empirical current-voltage temperature results (Section 5.3). Ta-

ble 4.1 summarizes the parameters and their typical values required to calculate the bulk thermal generation current. Using the values presented and the above formulae, the bulk thermal current density can be estimated to be $\sim 2.5 \times 10^{-11}$ A·cm^{-2}.

Table 4.1: Typical parameter values used to calculate the bulk thermal generation current in a a-Si:H photodiode [2].

Parameters	Symbol	Value	Units
Device temperature	T	313.15	K
Intrinsic layer thickness	t_i	5×10^{-5}	cm
Mobility Gap	E_μ	1.877	eV
Electron capture cross section	σ_e	1×10^{-15}	cm^{-3}
Hole capture cross section	σ_h	1×10^{-14}	cm^{-3}
Excitation rate prefactor	ω_0	1×10^{13}	s^{-1}
Transient depletion charge	Q_D	1.28×10^{-4}	C
Change in Fermi level position in i-a-Si:H	ΔE	0.2	eV

Voltage Dependence of Bulk Thermal Leakage

Although Equation 4.14 implies no voltage dependence for the steady state thermal generated current, empirical values state otherwise. Researchers have tried to explain this bias dependence by: an increase of generation centers [74], field enhanced emission processes [7], or electron-lattice interaction mechanism [75]. However, no conclusive theory states which component is the dominant cause.

Kramer et al. argue that the bias dependence in the width of the depletion region in the i-layer was small compared to the field enhanced conduction and should be ignored [7]. They argued that since most generation centers are located near E_{FD}, the activation energy of the reverse current should be bias independent. They also argue that in order for the increase in generation center theory to work, the de-

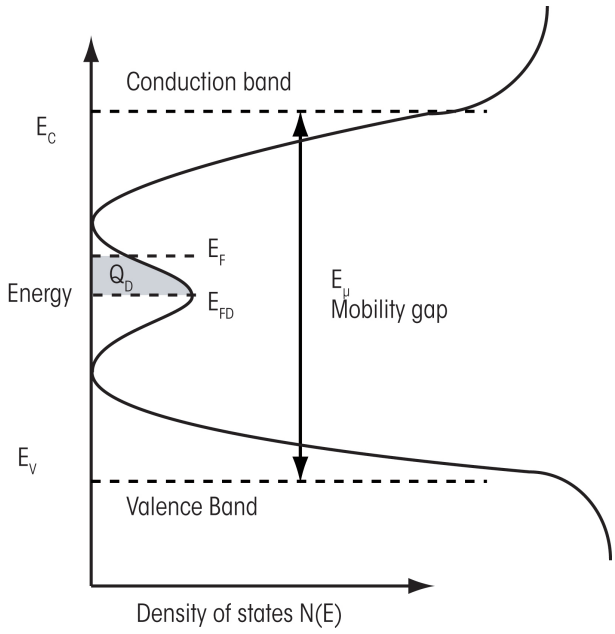

Figure 4.6: Density of states showing the depletion charge.

pletion charge should have a bias dependence similar to the current itself. However, this is not the case. The bias dependence of the depletion charge tends to be much weaker than the bias dependence of the current. Therefore, Kramer et al. suggested that field assisted excitation explains the bias dependence of dark reverse current. There are two field dependent emission mechanisms: Poole-Frenkel and thermally assisted tunneling. For electrons, if the particle was from an initially neutral defect ($D^{+/0}$) then the enhancement can be described by a Poole-Frenkel mechanism. On the other hand, if the trap was initially negative ($D^{0/-}$) then the enhancement is attributed to thermally assisted tunneling. Both of these conduction mechanisms are shown in Figure 4.7, where (a) illustrates the Poole-Frenkel emission and (b) the thermally assisted tunneling. For holes, the situation is reversed. The probability for thermally assisted tunneling (TAT) of electron emission from a trap E_t below

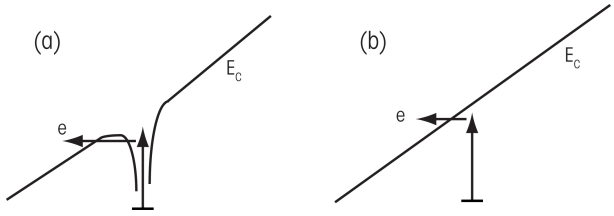

Figure 4.7: Field enhanced conduction mechanisms for electrons: (a) Poole-Frenkel and (b) thermally assisted tunneling [7].

the conduction band (E_C), $e_{TAT,e}(E_t, \overrightarrow{E})$, is given by:

$$e_{TAT,e}(E_t, \overrightarrow{E}) = \omega_0 e^{\left(\frac{E_C - E_t}{kT}\right)} + \int_{E_C}^{E_t} \frac{\omega_0}{kT} e^{\left(\frac{E_C - E_t + \delta E}{kT}\right)} P(\delta E, \overrightarrow{E}) d(\delta E). \tag{4.22}$$

In Equation 4.22, the first term refers to the thermal emission. The second term (the integral term) refers to the enhancement due to the escape probability via virtual states, located δE below the conduction band. The density of these virtual states, $P(\delta E, \overrightarrow{E})$, can be calculated with the Wentzel-Kramers-Brillouin (WKB) approximation as follows:

$$P(\delta E, \overrightarrow{E}) = e^{\left(-2\int_{d1}^{d2} \sqrt{\frac{2m^* q(2\pi)^2}{h^2}\left[V(x, \overrightarrow{E}) - E_t\right]} dx\right)}. \tag{4.23}$$

The above equation calculates the penetration of the conduction-band electron wave function through a triangular potential barrier. For Poole-Frenkel (PF) emission, the probability is given by:

$$\begin{aligned} e_{PF,e}(E_t, \overrightarrow{E}) &= \omega_0 e^{\left(\frac{E_C - E_t + \Delta E_{PF}}{kT}\right)} \\ &+ \int_{E_C}^{E_t + \Delta E_{PF}} \frac{\omega_0}{kT} e^{\left(\frac{E_C - E_t + \Delta E_{PF} + \delta E}{kT}\right)} P(\delta E, \overrightarrow{E}) d(\delta E). \end{aligned} \tag{4.24}$$

In Equation 4.24, ΔE_{PF} describes the energy barrier reduction due to the interac-

tion between charged trap and the electric field and can be expressed as:

$$\Delta E_{PF} = 2\sqrt{\frac{q\overrightarrow{E}}{4\pi\varepsilon_r\varepsilon_0}}. \tag{4.25}$$

The value $P(\delta E, \overrightarrow{E})$ for the Poole-Frenkel case is similar to the one found in Equation 4.22, except that the barrier height has changed. Similar equations can be derived for hole emission to the valence band.

The above mechanism work well individually in describing the conduction of single charges. However, when considering the carrier generation in the i-layer, the above two mechanisms need to be considered simultaneously. Figure 4.8 shows both potential mechanisms. Figure 4.8 (a) shows an initially negatively charged trap which emits an electron by thermal assisted tunneling. Then a hole is generated by Poole-Frenkel emission. Figure 4.8 (b) on the other hand shows an initially neutral trap which emits an electron via Poole-Frenkel emission and then generates a hole by thermal assisted tunneling. By using SRH statistics, the generation current in

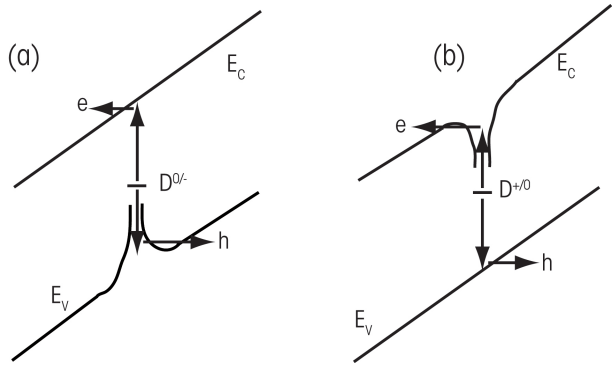

Figure 4.8: Carrier field enhanced generation: (a) thermally assisted tunneling and (b) Poole-Frenkel [7].

the i-layer for both mechanisms can be expressed as:

$$\begin{aligned} I_{0/-}(\overrightarrow{E}) &= d\int N(E)\left(\frac{e_{PF,h}(E,\overrightarrow{E})}{e_{PH,h}(E,\overrightarrow{E})+e_{TAT,e}(E,\overrightarrow{E})}\right)e_{TAT,e}(E,\overrightarrow{E})dE \\ I_{+/0}(\overrightarrow{E}) &= d\int N(E)\left(\frac{e_{TAT,h}(E,\overrightarrow{E})}{e_{TAT,h}(E,\overrightarrow{E})+e_{PF,e}(E,\overrightarrow{E})}\right)e_{PF,e}(E,\overrightarrow{E})dE \end{aligned} \tag{4.26}$$

To summarize, the field assisted enhancement from a charged defect can described by thermal assisted tunneling with an enhancement factor of $exp(-\beta_t\overrightarrow{E})$. If the particle was from an initially neutral defect, the enhancement can be described by a Poole-Frenkel mechanism and the enhancement will be of $exp(-\beta_p\overrightarrow{E}^{1/2})$. Assuming a uniform field, these field assisted mechanisms are a possible explanation for the observed voltage dependence of the thermal current. By taking into account these new factors, the bulk generation current equation can be rewritten as:

$$J_b\left(\overrightarrow{E}\right) = J_{th}\exp\left(\beta_t\left|\overrightarrow{E}\right|\right)\alpha_p\exp\left(\beta_p\sqrt{\left|\overrightarrow{E}\right|}\right)\exp\left(\beta_{pd}\sqrt{\left|\overrightarrow{E}\right|}^{3}\right), \tag{4.27}$$

where $\overrightarrow{E}$, β_t, α_p, β_p, and β_{pd} are the average electric field across the intrinsic layer, the tunneling constant, the Poole-Frenkel exponential prefactor, the Poole-Frenkel exponential constant, and the partial depletion exponential constant respectively. The $\beta_p d$ term is to account for the fact that full depletion is not formed at low reverse bias.

Edge Leakage

Another source for the reverse bias dark current is the edge or peripheral leakage current and it is particularly significant for smaller devices. Schiff et al. showed that there exists a bias dependence for the reveres bias current [8]. Figure 4.9

shows this dependence for 400×400 μm^2 diodes. By measuring the reverse bias current of diodes of different sizes, it was concluded that the variability observed can be attributed to the peripheral current. The center current straight line is the predicted contribution from the bulk current. The variability observed is largely attributed to the process variation in the etching and passivation during fabrication of the device. Unpassivated sensors tend to have large leakage currents due to their high sensitivity to ambient atmosphere [1]. The edge leakage component can be attributed to the increased defect density at the photodiode junction sidewalls. The increase in defects can be attributed to the damage resulting from the dry reactive ion etching (RIE) process. Another possible cause for the edge leakage current is the presence of surface states due to the change in material at the interface.

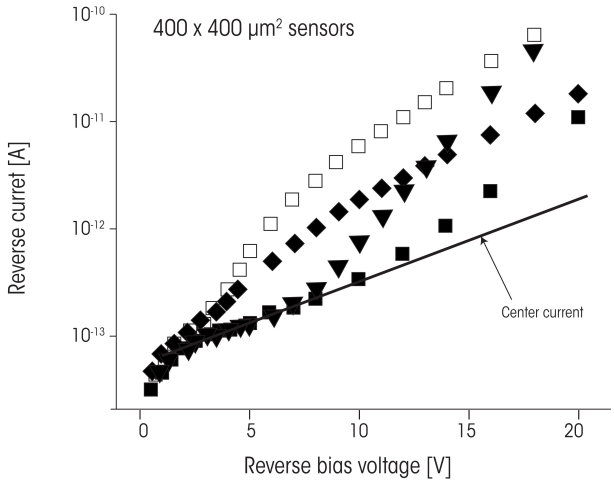

Figure 4.9: Variation of reverse bias current due to edge leakage. [8]

The total diode current, I_{total}, including both bulk, J_B (A·cm^{-2}), and peripheral component, G_P (A·cm^{-1}), for a square diode is:

$$I_{total} = J_B d_s^2 + 4 G_P d_s, \tag{4.28}$$

where d_s is the edge length of the diode. By measuring square diodes of different sizes, J_B and G_P can be easily extracted. The peripheral component is bias dependent as well as temperature dependent and can be empirically modeled as:

$$\begin{aligned} & G_P(T, V_{bias}) = A(T)V_{bias}^2 + B(T)V_{bias} + C(T) \\ & = (A_2T^2 + A_1T + A_0)V_{bias}^2 + (B_2T^2 + B_1T + B_0)V_{bias} \\ & +(C_2T^2 + C_1T + C_0) \end{aligned} \tag{4.29}$$

Contact Injection Generation

Note that Equation 4.28 does not include the charge injection component, since it is usually considered to be negligible in n-i-p diodes. The contact injection component depends highly on the barrier height of the contacts. A low barrier height means that the contact injection dominates over the other components. In Schottky barriers, this is indeed the case [69]. However, for n-i-p devices, the thermal bulk component dominates due to the high barrier height and the charge injection can usually be ignored [74] [76].

4.2 Capacitance

The capacitance is not only important in determining the response time of the photodiode, but also determines the amount of charge that can be stored. Section 3.4 presented a theoretical equation for the total capacitance of a photodiode. However, Equation 3.16 requires the knowledge of the distribution of mid-gap states, which is difficult to extract empirically. A more practical equation derived from the conventional parallel plate capacitance formula can be used instead to model

the capacitance of the photodiode. The equation can be expressed as:

$$C_{photodiode} = \frac{\varepsilon A}{t_i} = \frac{\varepsilon_0 \varepsilon_{a-Si:H} A}{t_i}, \tag{4.30}$$

where ε_0, $\varepsilon_{a-Si:H}$, A, t_i are the permittivity of free space, the relative permittivity of intrinsic a-Si:H, the photodiode area, and the thickness of the intrinsic layer in the photodiode respectively.

4.3 Quantum Efficiency

The quantum efficiency of the photodiode depends on several processing parameters, including the thickness of the p-layer, the thickness of the anti-reflection coating, and the thickness of the intrinsic layer. These parameters can be optimized to maximize the quantum efficiency at a specific wavelength of impinging light. The quantum efficiency, η_{QE}, is a function of λ and can be experimentally fitted with a fourth order polynomial as:

$$\eta_{QE}(\lambda) = A_4\lambda^4 + A_3\lambda^3 + A_2\lambda^2 + A_1\lambda + A_0 \tag{4.31}$$

Once the quantum efficiency of the photodiode is modeled, the generated photocurrent, $I_{generated\_ph}$, can be expressed by the following equation:

$$I_{generated\_ph} = q\eta_{QE}\phi_{photon}A, \tag{4.32}$$

where q, η_{QE}, ϕ_{photon}, and A are the elementary charge, quantum efficiency, photon flux, and area of the photodiode respectively. This equation is based on Equation 3.1 as presented in Section 3.2.

4.4 Summary

Following the groundwork established in the previous sections, this chapter introduces an empirical model for the a-Si:H photodiode. The model is composed of a diode, a capacitor in parallel, and a current source. The diode is used to model the current-voltage characteristics of the photodiode. The forward bias and the reverse bias regions are modeled separately. The forward bias region is further separated into three areas: low, medium, and high bias. The low bias region behaves like an ideal diode. The medium bias region experiences a current reduction due to a series resistance. The high bias region has a current power law relationship to voltage due to space-charge limited current. The reverse bias current is composed of a bulk thermal generation component, edge leakage component, and charge injection component. The bulk component depends on the defects in the intrinsic layer and the temperature. The edge component comes from the increased defect density at the photodiode junction sidewalls and scales with the perimeter. With good blocking contacts, the contact injection component can be neglected. The capacitor in the model is to take into account the capacitance of the diode and can be modeled using a simple parallel plate capacitor equation. Finally, the current source is to simulate the photocurrent generated by the photodetector under illumination. The current generated is proportional to the photon flux, the quantum efficiency and the area of the photodiode.

Chapter 5

Model Validation

Model validation is often overlooked, but it is the most important step in a model building sequence [77]. Model validation determines how well a model fits the empirical data. A model that does not fit the data cannot be used to provide good answers to the underlying phenomenon under investigation. There are several tools that can be used to validate a model. A common and simple method is to use graphical residual analysis. The residual is the difference between the measured data and the predicted response. The residual for the i^{th} observation can be mathematically expressed as:

$$e_i = y_i - f\left(\overrightarrow{x_i}, \overrightarrow{\beta_i}\right), \tag{5.1}$$

where y_i is the response in the i^{th} observation, the quantity that the model is supposed to simulate. The mathematical function f represents the model and is composed of a list of variables, $\overrightarrow{x_i}$, and the appropriate parameter list, $\overrightarrow{\beta_i}$. If the residuals appears to behave randomly, then it can be concluded that the model fits the data well. On the other hand, if non-random behavior is observed in the

residual data, further improvements on the model is possible. This is due to the fact that measurements will include random errors that are not taken into account by the model.

In short, following the presentation of the empirical model in Chapter 4, this chapter aims at validating it. First, a description of the test devices is presented as well as their fabrication method. Then, the parameters of the model equation are extracted. Finally, the model is validated by comparing the theoretical model with the measured results and calculating the residuals.

5.1 Sample Preparations

A series of segmented n-i-p photodiodes with varying sizes and geometries were fabricated in a MVSystems^{TM} multi-chamber deposition tool, shown in Figure 5.1. The multi-chamber structure includes a load-lock chamber, an insulation-transport

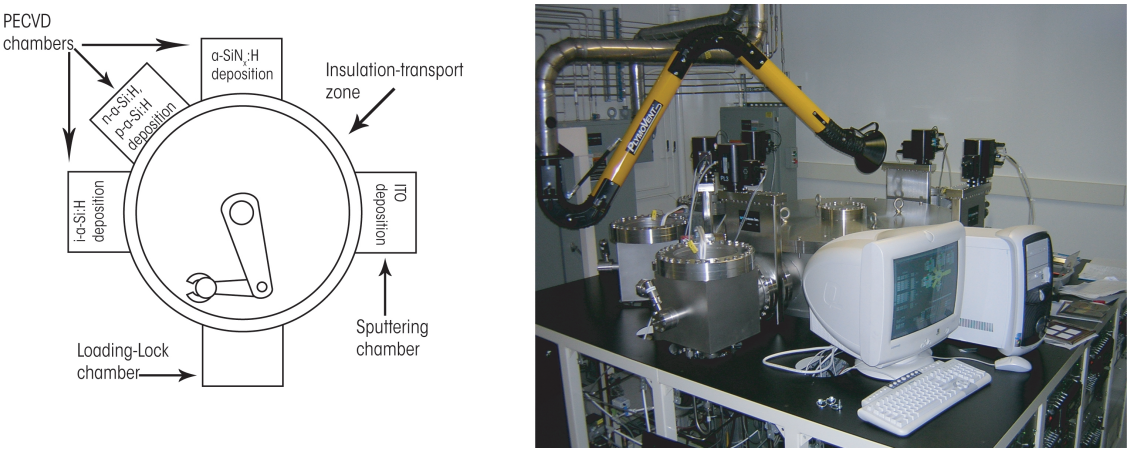

Figure 5.1: Schematic and photograph of the MVSystems^{TM} multi-chamber deposition tool.

zone with a robotic arm, and four process chambers. Intrinsic, negatively doped, positively doped a-Si:H (i-a-Si:H, n-a-Si:H, p-a-Si:H) semiconductor layers, and amorphous silicon nitride passivation layers were deposited using standard plasma-enhanced chemical vapor deposition (PECVD). On the other hand, the indium tin oxide (ITO) was deposited via magnetron sputtering. All the above materials were deposited in separate process chambers to avoid cross-contamination. The base pressures of the process chambers and insulation-transport zone are 10^{-6} - 10^{-7} Torr and 10^{-5} Torr respectively. The process chambers can be regulated at temperatures between 25 and 400 °C. 13.56 MHz RF generators with output power of 100 and 600 W were used in the system to support the plasma required for PECVD and sputtering processes respectively [3].

Intrinsic a-Si:H was deposited with hydrogen diluted or pure silane SiH_4 gas. To obtain n-a-Si:H and p-a-Si:H, gas phase doping with hydrogen diluted phosphine (PH_3/H_2) and tri-methyl boron (TMB/H_2) were used respectively. ITO was sputtered using Ar-O_2 plasma. Other metal layers, such as Aluminium (Al), Chromium (Cr), and Molybdenum (Mo) were sputtered on at room-temperatures with Argon (Ar) plasma. The thickness of deposited films and mechanical stress were measured using a Dektak^{TM} surface profiler [3].

5.1.1 Deposition Optimization

Dr. Y. Vygranenko and Dr. K.H. Kim determined the different deposition parameters required to obtain the lowest defect density for the i-aSi:H layer and the optimal doping level for the p-aSi:H layer [78] [79]. An intrinsic layer that is low in defects can reduce the thermal generation current, and thus reducing the dark current. An optimized p-layer reduces the charge injection, and thus minimizing

the contribution of the p/i interface.

The defect density of the deposited layer can be determined by a number of techniques, such as: capacitance-voltage measurements, electron spin resonance (ESR), constant photocurrent method (CPM), photodeflection spectroscopy (PDS), and field-effect measurements [1]. The above methods require special sample preparation, specific equipment and lengthy measurement, which are not always available in a pilot line. A more practical approach is to measure the photoconductivity or other device parameters and correlate these results to the defect density. For example, photoconductivity is approximately inversely proportional to defect density [1]. Table 5.1 summarizes the optimal process conditions used in the Giga2Nano Laboratory to fabricate device grade a-Si:H at 220 °C.

Table 5.1: Optimized deposition parameters for device-quality grade i-aSi:H [3].

Parameter	Value	Unit
Silane (SiH_4) gas flow	20	sccm
Gas pressure	400	mTorr
RF power	2	W
Deposition rate	1.80	$\mathring{A}\cdot s^{-1}$

Doping was achieved via gas phase doping. n-aSi:H and p-aSi:H layers were grown with SiH_4 and the addition of PH_3 and TMB respectively. The doping efficiency in a-Si:H with this procedure is rather low. Note that whereas in c-Si, doping is substitutional, meaning that a Si atom in the lattice is replaced by a dopant atom, this is not the case in a-Si:H. Doping in a-Si:H is defined by the coordination of the impurity atom. Doping atoms can be either three-fold or four-fold coordinated. Only four-folded coordinated atoms are electrically active and

act as dopants. The doping efficiency in a-Si:H, η_{doping}, is defined as:

$$\eta_{doping} = \frac{N_4}{N} = \frac{N_4}{(N_3 + N_4)} = \frac{(n_{bandtail} + n_{defect})}{N}, \tag{5.2}$$

where N_4, N_3, and N are the number of four-fold coordinated, three-fold coordinated and total number of impurity atoms. The variables $n_{bandtail}$ and n_{defect} refer to the densities of excess carriers in the band tail states and defect (or deep) states that can take on extra electrons due to doping.

For a-Si:H photodiodes, a high enough built-in potential (achieved by doping) is required to prevent charge injection. However, high doping concentration in the p-layer leads to high defect density and hence increases optical losses and decreases quantum efficiency. Furthermore, the impurity atoms can diffuse into the intrinsic layer at low temperatures, which creates deep localized states near the p-i interface. Localized sates at the interface can act as generation-recombination centers and increase dark leakage current. Therefore, optimization of the doping conditions is of primary importance to the quality of the photodiode. Table 5.2 summarizes the optimized parameters used in depositing doped a-Si:H layers.

Table 5.2: Optimized doping parameters for doped a-Si:H [3].

Parameter	N type doping	P type doping	Unit
SiH_4 gas flow	20	20	sccm
PH_3 gas flow	5	0	sccm
TMB gas flow	0	10	sccm
Pressure	400	400	mTorr
RF power	2	2	W
Deposition rate	1.3	2.6	$\mathring{A}\cdot s^{-1}$
Dark Conductivity	$\sim 1\times10^{-2}$	1.59×10^{-6}	$S\cdot cm^{-1}$

5.1.2 Test Sample Structure

For the measurements, square diodes of five different sizes were fabricated and tested. The diode photosensitive areas were: 126×126 μm^2, 250×250 μm^2, 500×500 μm^2, 1×1 mm^2, and 2×2 mm^2. Figure 5.2 shows a cross-sectional diagram of the fabricated photodiodes. The photodiodes were deposited via standard PECVD at 220 °C as described in Section 5.1

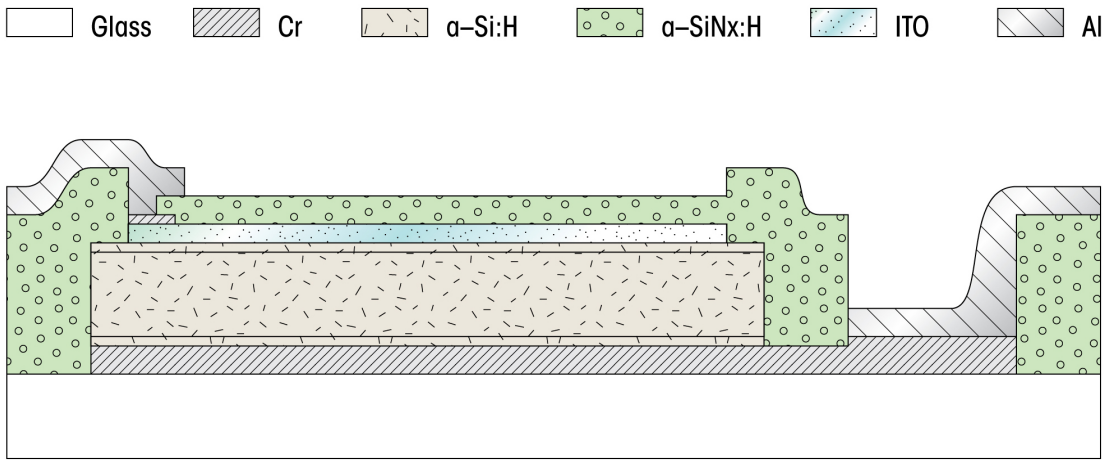

Figure 5.2: Schematic of cross section of the fabricated a-Si:H nip photodiodes [9].

The undoped a-Si:H i-layer is 500 nm in thickness with 40 nm heavily doped n+ (a-Si:H:P) and p+ (a-Si:H:B) layers as ohmic contacts. Photodiode junctions are isolated from one another using reactive ion etching (RIE) via SF_6 plasma, and the junction sidewalls are passivated using non-stoichiometric a-SiNx:H. A 80 nm thick indium-tin-oxide (ITO) layer is deposited on top of the p+ layer as the transparent conductive oxide (TCO). Cr and Al are sputtered as the bottom and top contact metals, respectively.

5.2 Measurement Techniques

The widespread use of amorphous materials has prompted the need for a basic understanding of their physical characteristics. For this purpose, many measurements techniques have been developed. Techniques that characterize current-voltage, capacitance-voltage, quantum efficiency, and other physical properties have been developed, since each measurement technique has its advantages and drawbacks. This section uses some standard and innovative techniques to obtain the necessary parameters needed to model the a-Si:H photodiode. More specifically, the methodology used to obtain the current-voltage characteristics, capacitance-voltage characteristics as well as quantum efficiency are summarized here.

5.2.1 Current-Voltage Measurements

Room temperature and high temperature current-voltage (I-V) measurements were obtained using a Keithley^{TM} 4200 Semiconductor Characterization System with Keithley^{TM} Remote Preamplifiers. The test system for room temperature measurement is shown in Figure 5.3. The room temperature current-voltage system uses an AttoGuard^{TM}MicroChamber as the test chamber and four Cascade^{TM} Microtech Precision Positioners for the probe tips. The device under test (DUT) is loaded from the side onto a chuck. The chuck uses suction to hold the sample in place. After loading the sample, the elevation lever is released to raise the sample to the desired height. The chuck can be rotated and translated using knobs located next to the loading bays. The coarse adjustments are made by visual inspection from an observation window. Once the coarse positioning adjustments are made, the probe tips can be accurately positioned at the desired locations using the Microtech Pre-

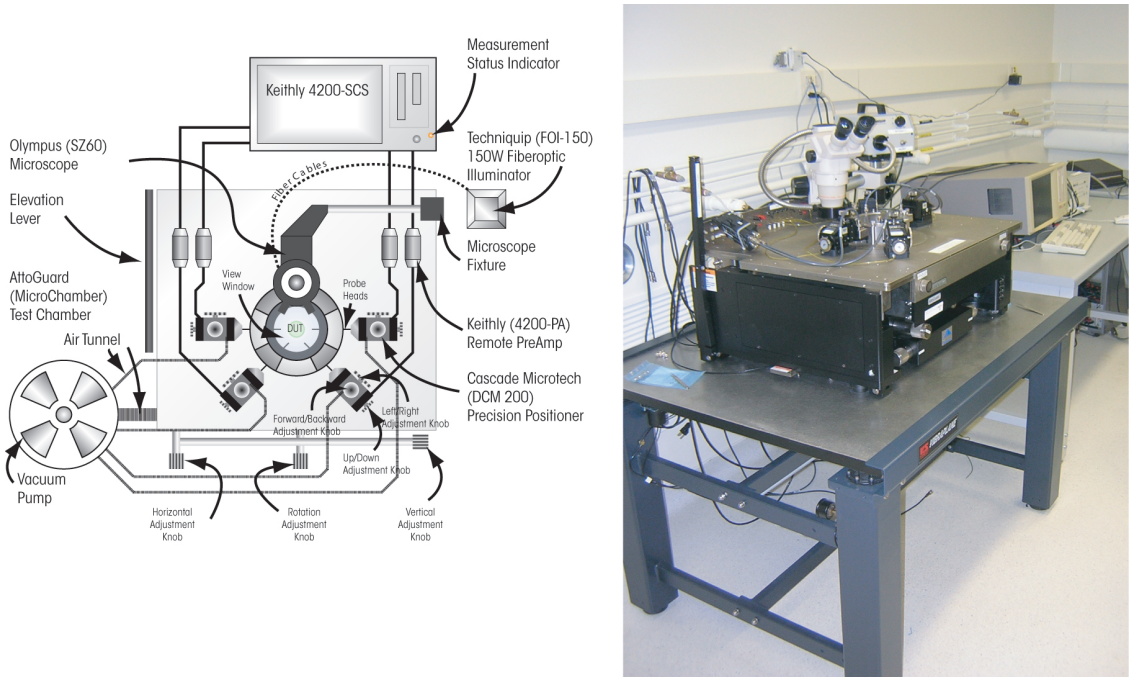

Figure 5.3: Schematic [10] and photograph of the room temperature I-V measurement system.

cision Positioners and a Olympus^{TM}microscope. The microscope is illuminated by a 150 Watts Techniquip^{TM} FOI-150 light source. The Microtech Precision Positioners allow for precise x, y, and z displacement of probe tips. In particular, the lowering of the tips (negative z displacement) is of critical importance, since both the probe tips and the sample are sensitive to the amount of stress applied. The probe tips send their signal to the semiconductor parameter analyzer via triaxial cables. There are also four Keithley^{TM} 4200-AP Preamplifiers to boost the signal coming from the probe tips.

High temperature I-V measurements were done in a similar apparatus of that of room temperature. The setup is shown in Figure 5.4. To regulate the temperature, dry air is regulated by a Temptronic^{TM} TP03000 System, which feeds the regu-

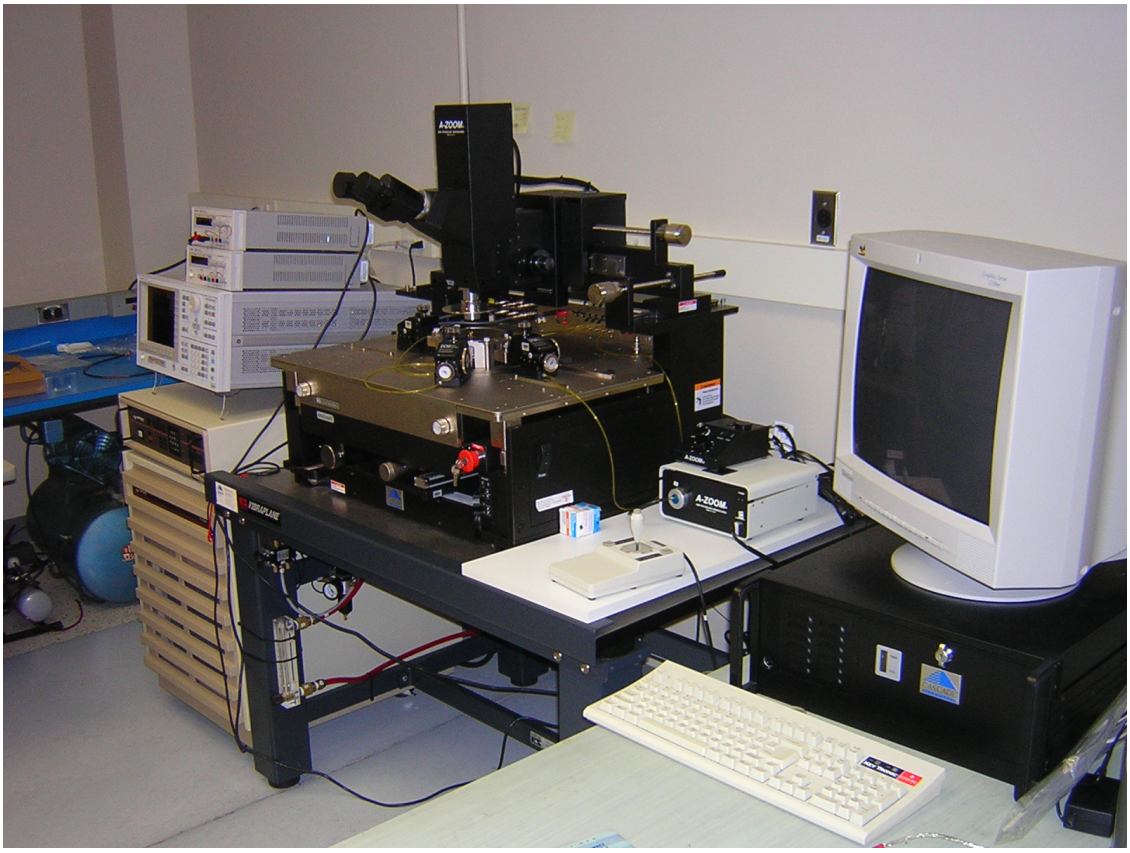

Figure 5.4: Photograph of the high temperature I-V measurement system.

lated dry air through a system of tubes surrounding the chuck. The test chamber apparatus used is similar to the room temperature system, except for three major differences. First, the chuck is not moved manually, but rather by a computer controlled motorized Cascade™ positioning system controlled by either a mouse or a joystick. The speed and range of the movement can be set from the computer to allow for fine adjustments. Second, instead of using a standard microscope to align the probe tips, an A-Zoom™ microscope system is used. The A-Zoom™ microscope is also connected to the computer and allows for the instant capture of images. Third, the probe tips are mounted on top of Cascade™ DCM 200 Series

Precision Positioners. The positioners operate similarly to the Microtech^{TM} one, except that they fit different probe tips.

In addition, both systems are physically isolated using Kinetic^{TM} Systems Vibraplane. In essence, the probe stations float on top of a raised air table to reduce the amount of ambient vibration. This is important, since small vibrations can cause stress on the sample and hence modify the measured current. In order to measure the dark current, the test chamber is isolated using a metal cover in both systems. In addition to turning off the lights in the test room, a black blanket is used to cover the whole system to further reduce the amount of photons impinging the sample.

The *I-V* characteristics of different photodiode sizes were measured between room temperature and 80 °C, under dark conditions. The photodiode biasing voltage was swept from 1 V to -5 V in 50 mV steps. The trapped charges in the bulk a-Si:H were removed by applying a reverse bias of -1 V for 60 seconds prior to the start of each sweep. The forward and reverse bias characteristics were measured separately. In addition, the current-voltage experiments spanned several days. The measurement parameters are summarized in Table 5.3 below.

To minimize temperature drift when performing high temperature measurements, a significant amount of time was allowed for stabilizing at the target temperature. Current readings at low temperatures and small-area photodiodes challenge the sensitivity limit of the measurement system ($\sim$ 10 fA) and generally yield a noisier reading. To obtain more accurate results, six small photodiodes of dimensions of 125 μm on a side were connected together to increase the measured current levels. It is assumed that each photodiode in the array will have very similar *I-V* characteristics. The flow of cooling gas can cause small vibrations of the test

Table 5.3: Summary of current-voltage measurement parameters used.

Parameter	Value	Unit
Measured temperature range	293.15 to 353.15	K
Biasing range	-5 to 1	V
Bias steps	50	mV
Current range	Auto	N/A
Current compliance	1	mA
Measurement speed	Normal	N/A
Delay factor	1	N/A
Filter factor	1	N/A
Sweep delay	2	s
Hold Time	60	s
Temperature stabilization wait time	30	mins

platform inducing stress variations on the sample and introducing additional error components.

5.2.2 Capacitance Measurements

The capacitance-voltage characteristics were measured using an Agilent™ 4284A Precision LCR meter. The device under test was placed inside the same probe station used for room temperature I-V measurements. The Keithley™ 4200 Semiconductor Characterization System was used to interface with the LCR meter and to readout the gathered data. Table 5.4 summarizes the parameters used to perform the capacitance-voltage measurements.

Table 5.4: Summary of capacitance-voltage measurement parameters used.

Parameter	Value	Unit
Voltage sweep range	-5 to 0	V
Sweep voltage step size	200	mV
Oscillator voltage level	100	mV
Measurement frequency	1 to 10	kHz
Range	Auto	N/A
Integration time	Long	N/A
Measurement model	Series model	N/A

5.2.3 Illumination Response of the Photodiode

To measure the spectral response of the photodiode, the test setup shown in Figure 5.5 was used. The photocurrent of the photodiode was measured while it was exposed to beams of specific wavelengths. The test system was previously calibrated using a Newport™ 818-UV photodiode with a known spectral response. The measured photocurrent is normalized with the calibrated diode's photocurrent and the responsivity of the device under test can be extracted [10].

In the test apparatus, the light source used was an Oriel™ model 66181 illuminator with a halogen lamp. A lens focuses the light from the halogen lamp onto an optical chopper. The chopper modulates the light beam at a frequency f and is used for the phase-sensitive detection technique described further below. A Stanford Research Systems™ SR540 chopper controller controls the optical chopper's modulation frequency. An Oriel™ model 77200 monochromator uses diffraction gratings to disperse the incoming modulated light and by use of slits creates a beam with the desired optical spectrum. The gratings inside the monochromator are controlled by an Oriel™ model 20025 stepper motor controller. This quasi-

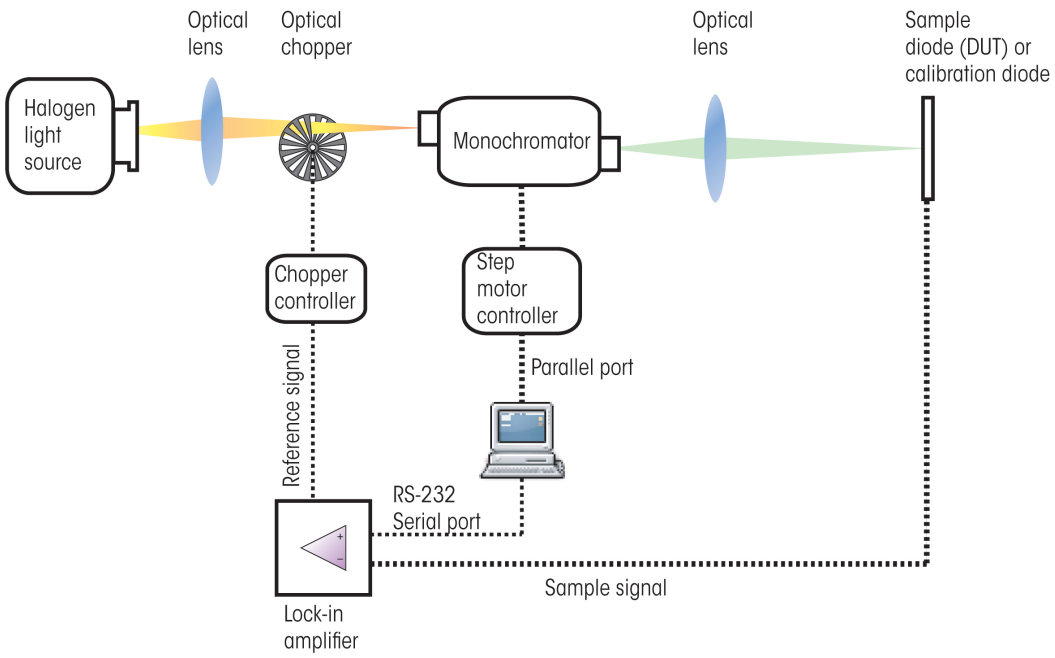

Figure 5.5: Schematic of the photodiode spectral response measurement system.

monochromatic beam is focused through a second lens onto the device under test. The measured photocurrent is fed into a Stanford Research System^{TM} SR830 DSP lock-in amplifier which can measure very low amplitude alternating current (AC) signals [80]. The final measured photocurrent signal was then saved into the computer via a RS232 serial port.

Phase Sensitive Detection

Although the photodiode sample used to characterize the spectral response is quite large, the output photocurrent was relative low when compared to the noise level. Using phase sensitive detection, accurate measurements of small signals can be measured even in the presence of noise sources many thousand times greater [81].

The SR830 DSP lock-in amplifier uses a phase sensitive detector (PSD) to measure small AC signals. A simplified PSD is presented in Figure 5.6.

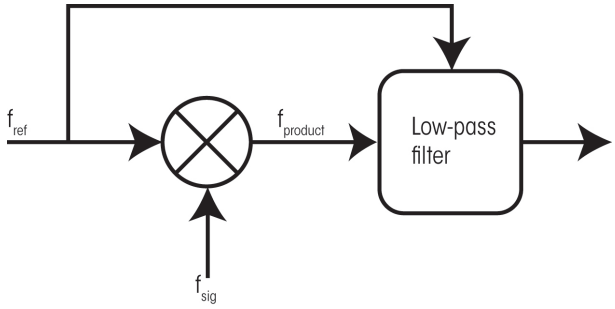

Figure 5.6: Schematic of a simplified phase sensitive detector.

The PSD takes in two signals, multiplies them together, and then passes the result through a low-pass filter. For example, given a measured signal, f_{sig} and a reference signal, f_{ref}:

$$\begin{aligned} f_{sig}(t) &= A_{sig}\cos(\omega_{sig}t + \theta_{sig}), \\ f_{ref}(t) &= A_{ref}\cos(\omega_{ref}t + \theta_{ref}), \end{aligned} \tag{5.3}$$

their product yields, :

$$\begin{aligned} &f_{product}(t) = f_{sig}(t) \times f_{ref}(t) \\ &= A_{sig}A_{ref}\frac{\cos[(\omega_{sig}-\omega_{ref})t+(\theta_{sig}-\theta_{ref})]+\cos[(\omega_{sig}+\omega_{ref})t+(\theta_{sig}+\theta_{ref})]}{2}, \end{aligned} \tag{5.4}$$

where A, ω, θ are the amplitude, frequency and phase of the signals respectively. As seen in Equation 5.4, the product of f_{sig} and f_{ref} can be expressed as the sum of two sinusoidal signals. One of the signals will have an angular frequency of $\omega_{sig} - \omega_{ref}$, called the difference frequency and the other signal will have an angular frequency

of $\omega_{sig}+\omega_{ref}$, called the sum frequency. Note that when both input signals have the same frequency, $\omega_{sig} = \omega_{ref}$, the signal with the difference frequency is constant. In addition, when the input frequencies are equal, the phase difference determines the constant output voltage. The maximum output voltage is achieved when the input signals are of the same frequency and phase.

The output signal from the PSD can be calculated, by applying the low-pass filter formula to the product of the input signals. The low-pass filter formula is:

$$V_{out} = \frac{V_{in}}{\sqrt{1+(\tau\omega)^2}}, \tag{5.5}$$

where V_{out}, V_{in}, τ are the output voltage, the input voltage and the time constant. Using superposition, the low-pass filter can be applied to the sum frequency signal and difference frequency signal independently to obtain the total filtered signal. Note that the signal with the difference frequency is unaffected for equal frequency input signals, while the signal with the sum frequency is heavily attenuated. In summary, a lock-in amplifier filters unwanted signals by modulating the source of the desired signal in a quiet frequency range, and then using this modulation as a reference frequency for the PSD, sources of noise can be heavily attenuated.

5.3 Parameters Extraction

The empirical model presented in Chapter 4 uses theoretical and empirical equations to describe the behavior of the a-Si:H photodiode. The equations presented tend to be very general and require some device specific parameters to accurately represent the photodetector fabricated at the Giga2Nano Laboratory. This section summarizes the data reduction and curve fitting methodologies used in obtaining

these parameters. Some of the equations presented previously will also be modified to account for these recently observed empirical behaviors. Although the process of data gathering, data reduction and curve fitting was performed several times, this section presents only the final conclusions derived from this cyclic process.

5.3.1 Current-Voltage Characteristics

As presented in Subsection 4.1.1, the forward and reverse I-V characteristics for the photodiode are modeled separately. Hence, different equations are used to describe both regions. The forward bias region is further separated into three sections: low, medium and high bias. The reverse bias in turn is the result of the bulk, edge and contact injection component, each determined by its own set of equations. The parameters for each equation will be extracted and summarized.

Forward Bias Photodiode Current

Figure 5.7 shows the measured current-voltage characteristics for varying diode sizes at 40 °C and the measured current-voltage characteristics for a 1×1 mm^2 photodiode at different temperatures. Note that the dark current doubles every 10 °C. For the low bias region, the diode follows the ideal equation presented in Equations 4.5 and 4.6. For any given temperature, $J_{0_{low}}$ and n can be extracted numerically by plotting the current-voltage measurements in a semi-log plot. A portion of the curve is then fitted to the following equation:

$$J_{F_{low}}(V) = J_{0_{low}} e^{\frac{qV}{nkT}} \tag{5.6}$$

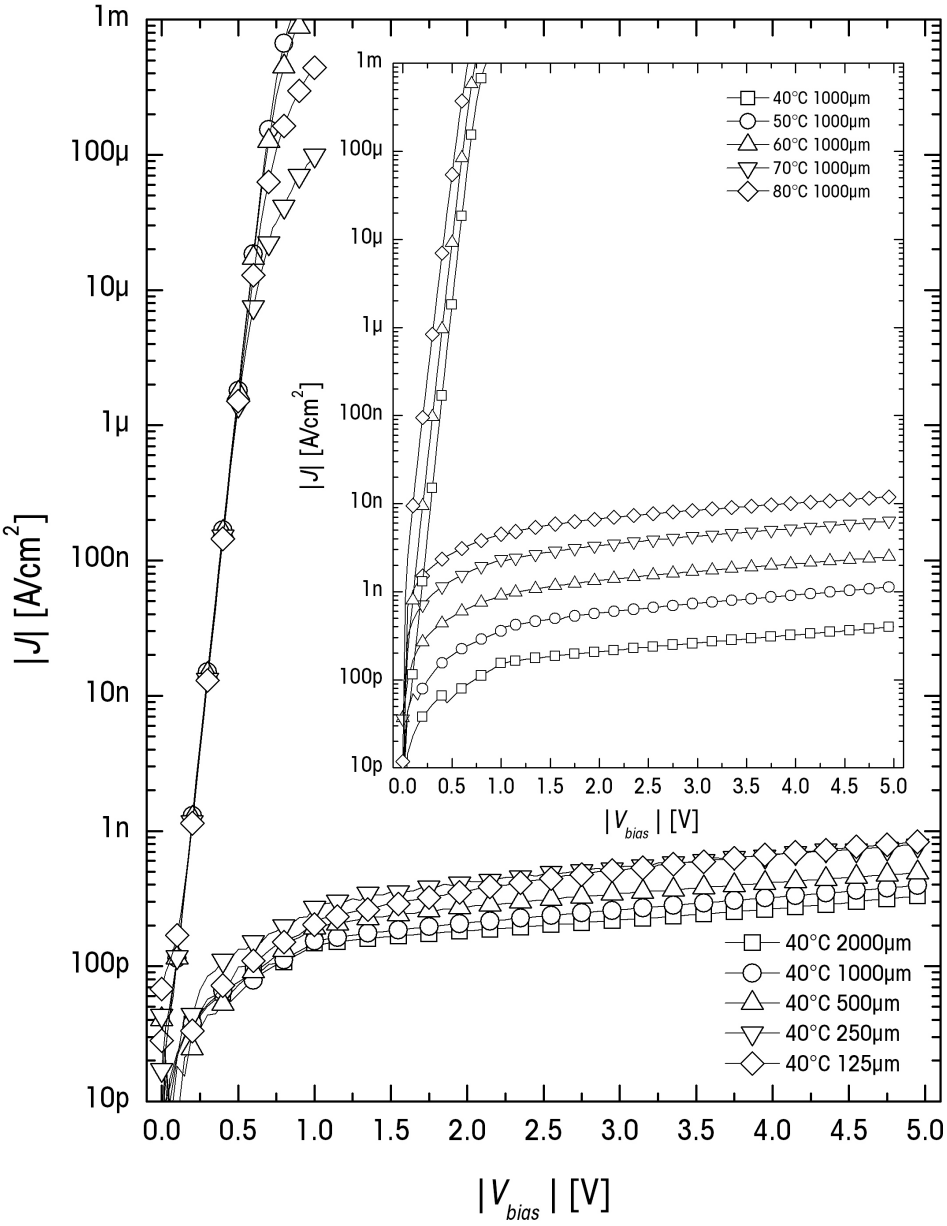

Figure 5.7: Measured $J-V$ characteristics at 40 °C for various sizes, and at different temperatures for a 1×1 mm^2 photodiode (inset) [9].

Note that Equation 5.6 is very similar to Equation 4.5 except for the minus one term. The main reason is that $J_{0_{low}}$ can be more easily extracted as the y-intercept, when Equation 5.6 is rewritten as:

$$\underbrace{\log|J_{F_{low}}(V_{bias})|}_{y} = \underbrace{\log|J_{0_{low}}|}_{B} + \underbrace{\frac{q}{nkT}\log|e|}_{M}\underbrace{V_{bias}}_{x}. \tag{5.7}$$

The minus one term can be dropped, since at higher biases (above 0.5 V), the exponential term dominates. From Equation 5.7, $J_{0_{low}}$ and n can be extracted using:

$$\begin{aligned} J_{0_{low}} &= 10^{B}, \\ n &= \tfrac{q\log(e)}{kTM}, \end{aligned} \tag{5.8}$$

where M refers to the slope in Equation 5.7. Once $J_{0_{low}}$ and n are obtained at each temperature, the $A_{0_{low}}$, $E_{a_{low}}$ values in Equation 4.7 can be extracted from the Arrhenius plot of $J_{0_{low}}$. Following the same methodology as before, Equation 4.7 can be rewritten as:

$$\underbrace{\ln|J_{0_{low}}(T)|}_{y} = \underbrace{\ln|A_{0_{low}}|}_{B} - \underbrace{E_{a_{low}}}_{M}\underbrace{(1/kT)}_{x}. \tag{5.9}$$

Similarly, the n_0 and δ_n values in Equation 4.7 can be easily extracted by performing a linear fit of the ideality values with respect to temperature.

$$\underbrace{n(T)}_{y} = \underbrace{n_0}_{B} - \underbrace{\delta_n}_{M}\underbrace{T}_{x}. \tag{5.10}$$

Figure 5.8 shows the extracted saturation current, and ideality factor, and activation energy for the forward bias region. The extracted activation energy averaged to ~ 0.85 eV, which is similar to the previous reported values [82] [83].

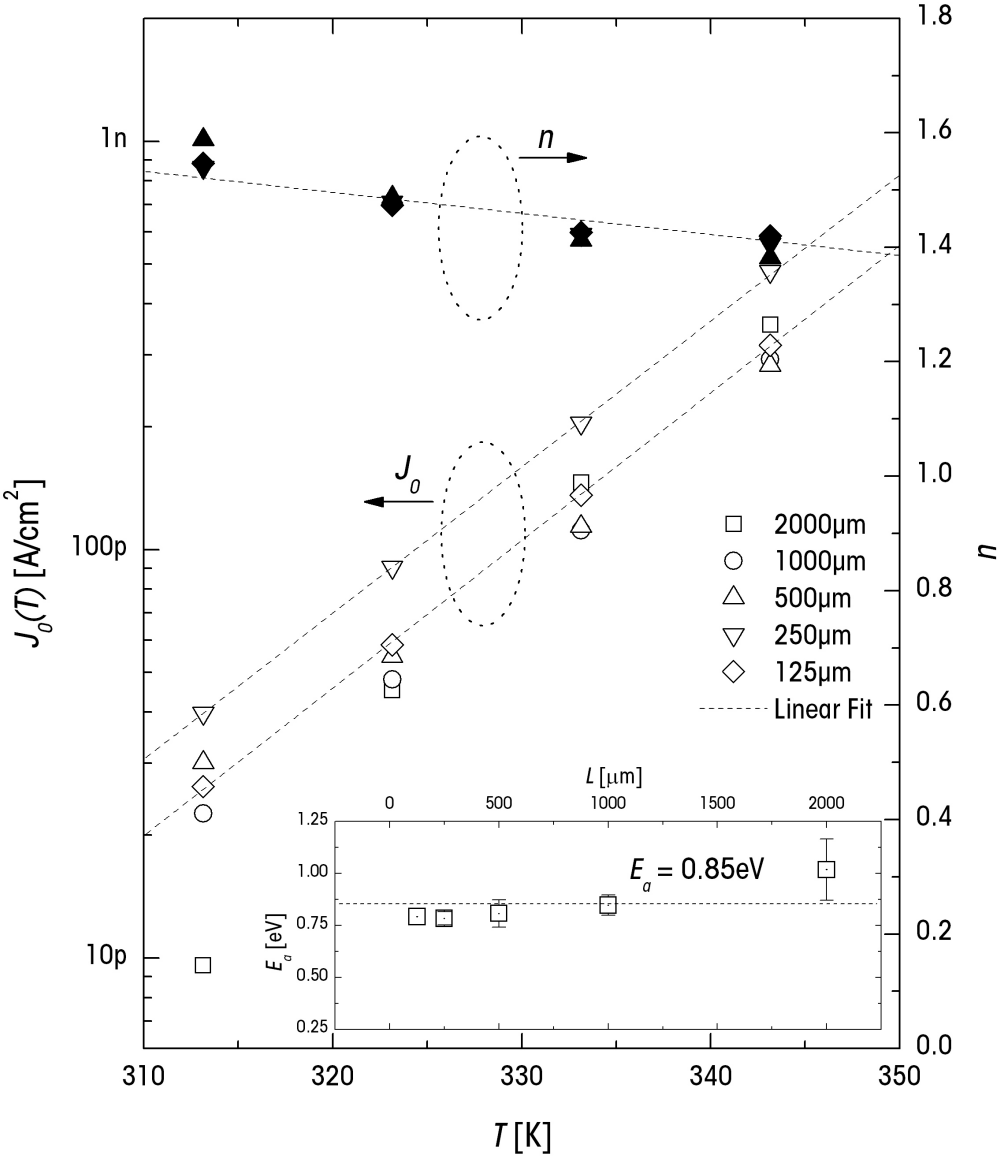

Figure 5.8: Extracted $J_{0_{low}}(T)$, $n(T)$, and activation energy (inset) for forward bias characteristics [9].

In the middle forward bias region, the current increases linearly instead of exponentially. This deviation from the ideal equation is caused by the series resistance of the diode. As mentioned previously, the series resistance can be caused by the contact resistance between the metal and the semiconductor, the resistivity of the semiconductor itself or due to the resistance of an external circuit. There are several methods proposed to extract the series resistance, R_s, in a diode. Usually it can be obtained by a linear fit of the forward I-V characteristics. By using Ohm's law, R_s can be calculated to be:

$$R_s = \frac{I_F}{V_{bias}} = \text{slope}. \tag{5.11}$$

However, this method relies on a reasonable initial estimate of the series resistance. In order to improve the accuracy of the estimations, Lyakas et al. suggest the addition of a known external resistance in series with the device during I-V measurements [84]. Ortiz-Conde et al. proposed an integration method, but the method is computation intensive and sometimes unreliable [85] [86]. Wong et al. developed a method using the proportional difference method [87]. Other methods include the use of optimization techniques [88]. Using the method described by Equation 5.11, the series resistance was estimated to be 407 $m\Omega$ for a 1×1 mm^2 diode.

For the high bias, the I-V characteristics of the photodiode no longer follow the ideal diode equation, but rather a power law relationship. To extract the parameters, Equation 4.10 can be rewritten as:

$$\underbrace{\log\left(J_{F_{high}}\right)}_{y} = \underbrace{\log\left(J_{0_{high}}\right)}_{B} + \underbrace{\gamma}_{M}\underbrace{\log(V_{bias})}_{x}. \tag{5.12}$$

Once $J_{0_{high}}$ and γ are extracted for all temperatures, the other parameters in Equation 4.11 can be extracted using equations similar to Equations 5.9 and 5.10. Table 5.5 summarizes the variables and the parameters used to model the forward bias current characteristics of the a-Si:H n-i-p photodiodes.

Table 5.5: Summary of extracted forward bias current parameters.

Parameter	Symbol	Value	Unit
Low bias saturation current pre-exponential factor	$A_{0_{low}}$	2.16×10^3	$\text{A}\cdot\text{cm}^{-2}$
Low bias saturation current activation energy	$E_{a_{low}}$	0.865	eV
Ideality factor at 0 Kelvin	n_0	1.91	N/A
Ideality factor reduction constant	δ_n	-1.12×10^{-3}	K^{-1}
Low bias weighting function smoothing parameter	$f_{p_{low}}$	30	N/A
Low bias weighting function center parameter	$f_{q_{low}}$	0.3	V
Series resistance	$R_{\square}$	40.7	$\Omega\cdot\text{cm}^{-2}$
High bias saturation current pre-exponential factor	$A_{0_{high}}$	145.1	$\text{A}\cdot\text{cm}^{-2}$
High bias saturation current activation energy	$E_{a_{high}}$	440×10^{-3}	eV
High bias exponent factor at 0 Kelvin	γ_0	19.0	N/A
High bias exponent factor reduction constant	δ_γ	45.0×10^{-3}	K^{-1}
High bias weighting function smoothing parameter	$f_{p_{high}}$	40	N/A
High bias weighting function center parameter	$f_{q_{high}}$	0.35	V

Reverse Bias Photodiode Current

As mentioned in Section 4.1.2, the reverse bias current is composed of the thermal generation current from the bulk, the current injection current from the doped contacts, and the edge leakage current from the exposed diode perimeter. For a photodiode with blocking contacts, it will be safe to assume negligible injection current and Equation 4.28 applies. By taking the reverse current-voltage characteristics of two square diodes of different edge (d_s) lengths, the bulk parameter (J_B) and the edge parameter (G_P) can be estimated. The above method assumes that for a given temperature and bias, J_B, G_P, and d_s remain constant. To minimize any possible measurement errors, three data sets and the least square method can be used to estimate the components. Figure 5.9 (a) shows the results of such extraction at 40 °C using square diodes with side lengths of: 1 mm, 250 μm, and 125 μm. Following the extraction of J_B and G_P, the bias and temperature dependence of both parameters can be obtained by curve fitting.

Using the parameters obtained, the reverse bias current of a 500×500 μm^2 diode can be calculated. As can be seen from Figure 5.9 (b), the extracted parameters produce a model that approximates the empirical data. However, the edge component is negative at low biases, which does not make physical sense. This discrepancy can be explained by curve fitting errors, measurement errors and unaccounted dark reverse bias current components, like the corner component.

An alternative linear regression method is to plot the current divided by the length ($G = I/d_s$) versus the length (d_s), which is shown in Figure 5.10. It can be seen from the plot that G varies linearly with respect to the length for values greater than 500 μm. By performing a linear fit, the slope will give the bulk component, J_B, and the y intercept will yield the edge component, G_P. The edge component can

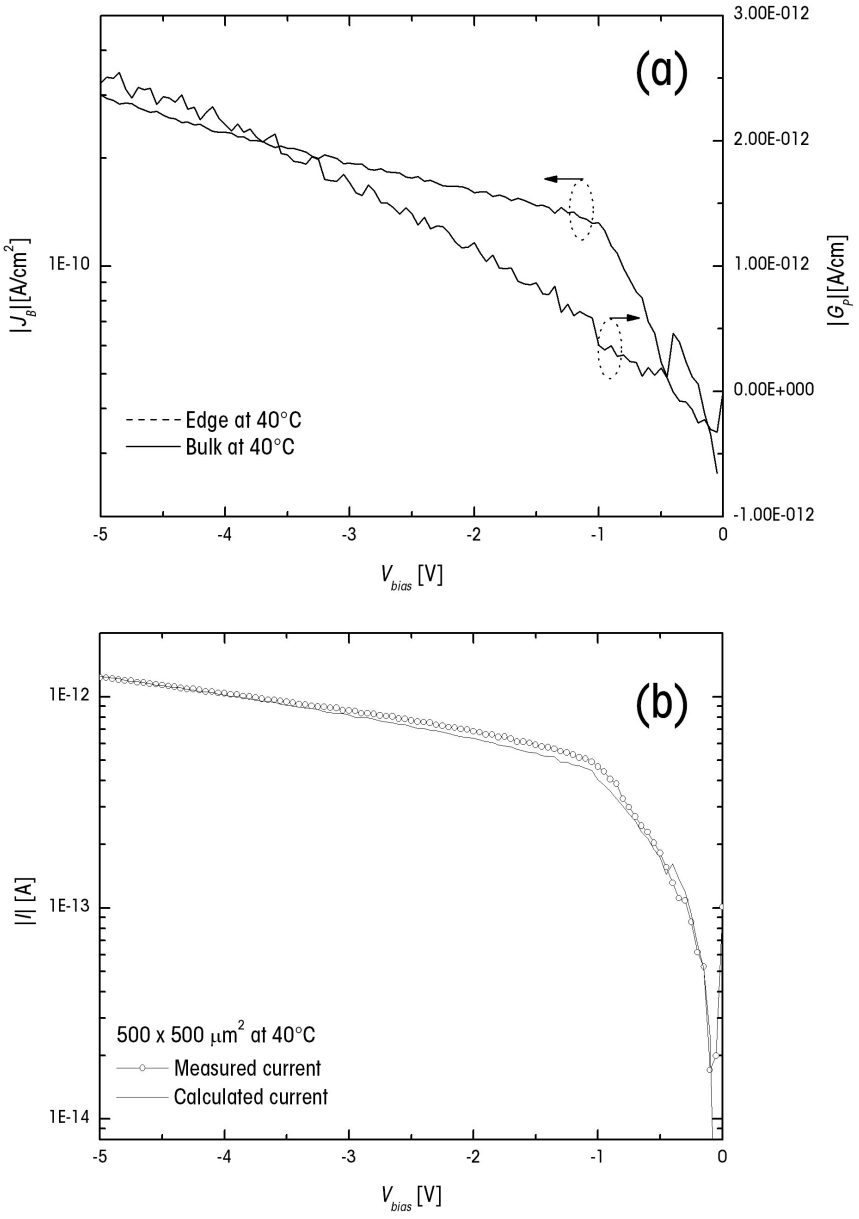

Figure 5.9: Graph showing the (a) extracted $J_B(V)$, $G_P(V)$ for dark reverse bias characteristics at 40 °C and (b) comparison between the calculated current and measured current.

also be obtained by subtracting the bulk component from the total diode current. Figure 5.11 shows the extracted bulk components versus temperature at different reverse bias voltages. The bulk component increases exponentially with temperature, which confirms the temperature dependence of the bulk component. Once the thermal bulk current is extracted at each temperature, the activation energy, $E_{a_{Bulk}}$, can be obtained from the Arrhenius plot. The average extracted activation energy is 0.91 $\pm$ 0.03 eV. By taking into account the temperature dependence of the mobility gap (E_μ) [89], the calculated E_μ from the activation energy agrees with the reported values 1.85 eV in device grade a-Si:H [1].

From Figure 5.11, the thermal bulk component scales approximately the same for all voltage bias, hinting that the activation energy is not strongly dependent on bias. Using the above, the thermal and field component of the bulk component can be decoupled. By assuming an uniform electric field across the intrinsic layer and using Equation 4.27, the bulk thermal current for an arbitrary temperature and bias can be empirically modeled by:

$$\begin{aligned} J_B(V_{bias}, T) &= J_0(T)\, e^{\left(-\beta_t \frac{V_{bias}}{t_i}\right)} \\ &= A_{0_{Bulk}} e^{\left(-\frac{E_{a_{Thermal}}}{kT}\right)} e^{\left(-\beta_t \frac{V_{bias}}{t_i}\right)}, \end{aligned} \tag{5.13}$$

where β_t is tunneling constant, t_i is the thickness of the intrinsic layer.

As mentioned previously, the edge component can also be graphically extracted as the intercept of the G versus sidelength graph or by solving a system of linear equation using Equation 4.28. Once the edge component is extracted it can be empirically modeled using Equation 4.29. In order to extract the various parameters in the equation. The edge component is first plotted versus the bias voltage and a second degree polynomial least-square fit is performed. Then, each variable from the

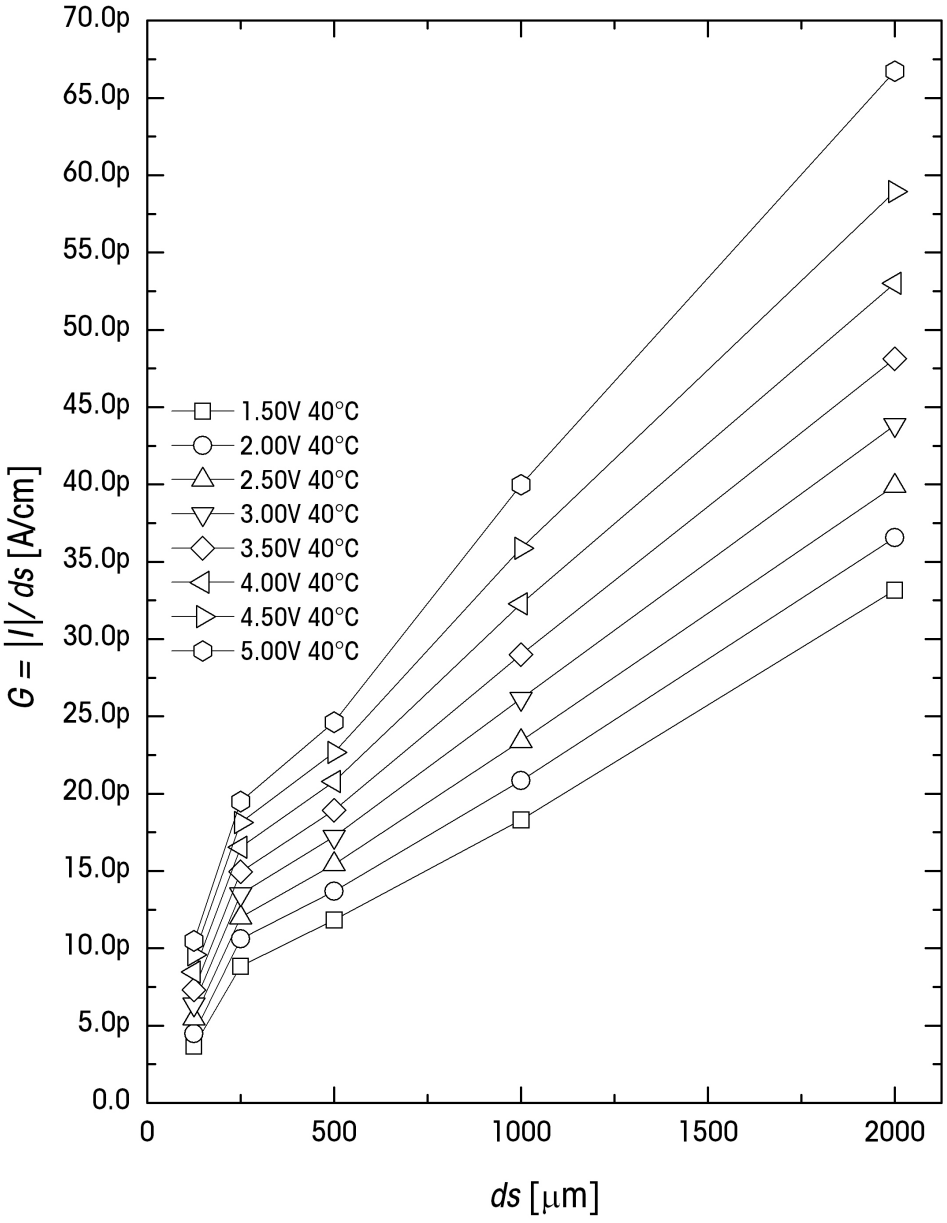

Figure 5.10: Measured current at 40 °C divided by photodiode sidelength plotted versus the sidelength to extract the reverse bias current components.

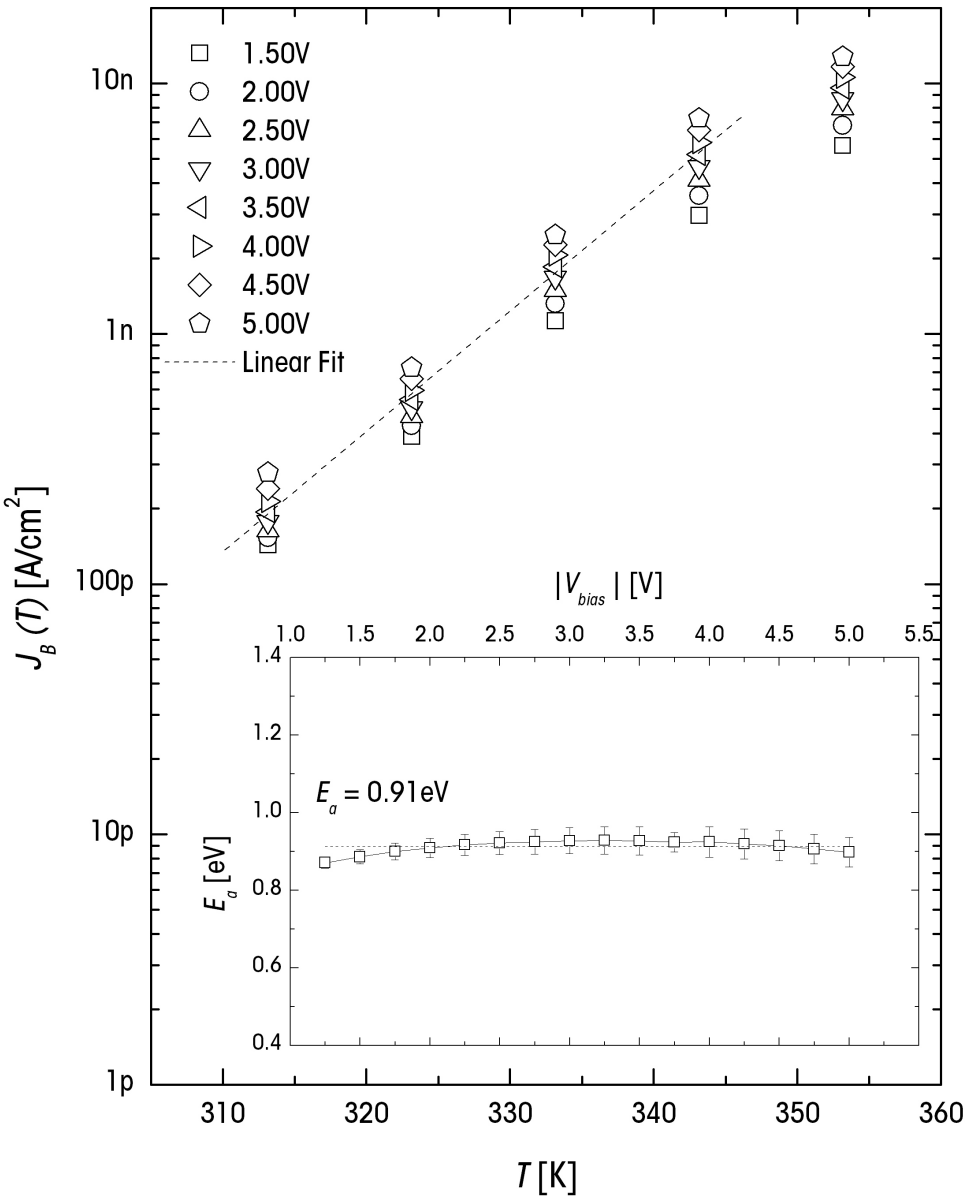

Figure 5.11: Extracted reverse bias thermal bulk current component and activation energy for the bulk component (inset).

fitted polynomial is plotted versus temperature and another polynomial regression is applied. The result is the extraction of the bias and temperature dependence parameters of the edge component.

Following the extraction of the bulk and edge parameters, the total reverse bias current can be calculated using Equation 4.28. Table 5.6 summarizes the parameters obtained from empirical data.

Table 5.6: Summary of extracted reverse bias current parameters.

Parameter	Symbol	Value	Unit
Bulk saturation current prefactor	$A_{0_{Bulk}}$	-51.5×10^{3}	$\mathrm{A{\cdot}m^{2}}$
Bulk saturation current activation energy	$E_{a_{Bulk}}$	0.913	eV
Tunneling factor	β_t	80.7×10^{-9}	$\mathrm{m{\cdot}V^{-1}}$
Intrinsic layer thickness	t_i	500	nm
Edge component fitting parameters	A_2	0	$\mathrm{A{\cdot}K^{-2}V^{-2}cm^{-1}}$
	A_1	0.329×10^{-12}	$\mathrm{A{\cdot}K^{-1}V^{-2}cm^{-1}}$
	A_0	-52.3×10^{-12}	$\mathrm{A{\cdot}V^{-2}cm^{-1}}$
	B_2	0	$\mathrm{A{\cdot}K^{-2}V^{-2}cm^{-1}}$
	B_1	42.8×10^{-15}	$\mathrm{A{\cdot}K^{-1}V^{-2}cm^{-1}}$
	B_0	19.0×10^{-12}	$\mathrm{A{\cdot}V^{-2}cm^{-1}}$
	C_2	-3.29×10^{-15}	$\mathrm{A{\cdot}K^{-2}V^{-2}cm^{-1}}$
	C_1	1.99×10^{-12}	$\mathrm{A{\cdot}K^{-1}V^{-2}cm^{-1}}$
	C_0	-0.299×10^{-9}	$\mathrm{A{\cdot}V^{-2}cm^{-1}}$

5.3.2 Capacitance Characteristics

Section 4.2 presented a capacitance model based on a parallel plate capacitance model. Shown in Figure 5.12 is the capacitance-voltage characteristics of a 1×1 mm^2 a-Si:H photodiode measured at 10 kHz.

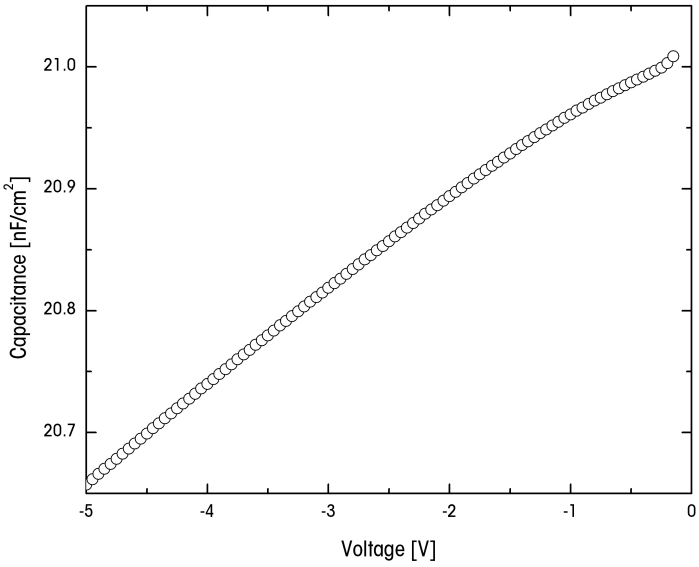

Figure 5.12: Capacitance-voltage characteristics of a 1×1 mm^2 a-Si:H photodiode measured at 10 kHz.

Using the values presented in Table 5.7, the capacitance of a 1×1 mm^2 n-i-p photodiode with a 500 μm thick intrinsic layer was estimated as 20.9 nF·cm^{-2}. This calculated capacitance agrees with the empirical results. From Figure 5.12, it can be seen that the capacitance stays fairly constant across the whole biased range. There is a slight deviation in the capacitance with bias, but the change is very small, indicating that full depletion is established even at low reverse biases. Empirically, a bias dependent correctional factor, δ_c, can be shown to improve the model. Note that the capacitance model is based on ideal parameters, it assumes optimal thickness and dielectric constant. A better fit would be to introduce a parameter C_0 that represents the actual capacitance. Equation 4.30 can be rewritten as:

$$C_{photodiode}(V_{bias}) = C_0 + \delta_c V_{bias} \tag{5.14}$$

Experimentally, it was observed that δ_c decreases with decreasing photodiode area as well. However, the capacitance variation is generally small in comparison with its actual magnitude and was not investigated further. Table 5.7 summarizes the extracted parameters related to the capacitance of the n-i-p photodiode.

Table 5.7: Summary of capacitance parameters of a a-Si:H n-i-p photodiode.

Parameter	Symbol	Value	Unit
Permittivity of free space	ε_o	8.85×10^{-12}	A^{2}s^{4}m^{-3}kg^{-1}
Relative permittivity of intrinsic a-Si:H	$\varepsilon_{a-Si:H}$	11.8	N/A
Photosensitive area of the diode	A	1	mm^2
Intrinsic layer thickness	t_i	500	nm
Capacitance correctional factor	δ_c	0.0763	nF·V·cm^{-2}
Fitted capacitance at 0 V	C_0	21.0	nF·cm^{-2}

5.3.3 Illumination Response

Shown in Figure 5.13 is the quantum efficiency of a Giga2Nano a-Si:H n-i-p photodiode. The absorption coefficient at long wavelength decreases, since the incoming photons have energy below the band gap energy. This in turn decreases the quantum efficiency at longer wavelengths. On the other hand, the decrease at short wavelength is due to the absorption of light by the upper doped layers and transparent conductors. Optimized a-Si:H diodes are most sensitive to green light, since their peak quantum efficiency occurs around 500 to 600 nm. For the Giga2Nano fabricated photodiode, the peak occurs at 560 nm with a quantum efficiency value of 0.77. Equation 4.31 suggests the use of a fourth order polynomial to fit the curve. The parameters extracted are summarized in Table 5.8 below. The parameters were extracted by polynomial regression of the measured data.

Table 5.8: Summary of quantum efficiency parameters of a-Si:H.

Parameter	Value	Unit
A_0	32	N/A
A_1	-0.25	nm^{-1}
A_2	750×10^{-6}	nm^{-2}
A_3	-0.93×10^{-6}	nm^{-3}
A_4	410×10^{-12}	nm^{-4}

5.4 Comparison and Analysis

The validation of the model usually involves quoting the coefficient of determination, R^2. The R^2 statistic is a numerical method for model validation and it

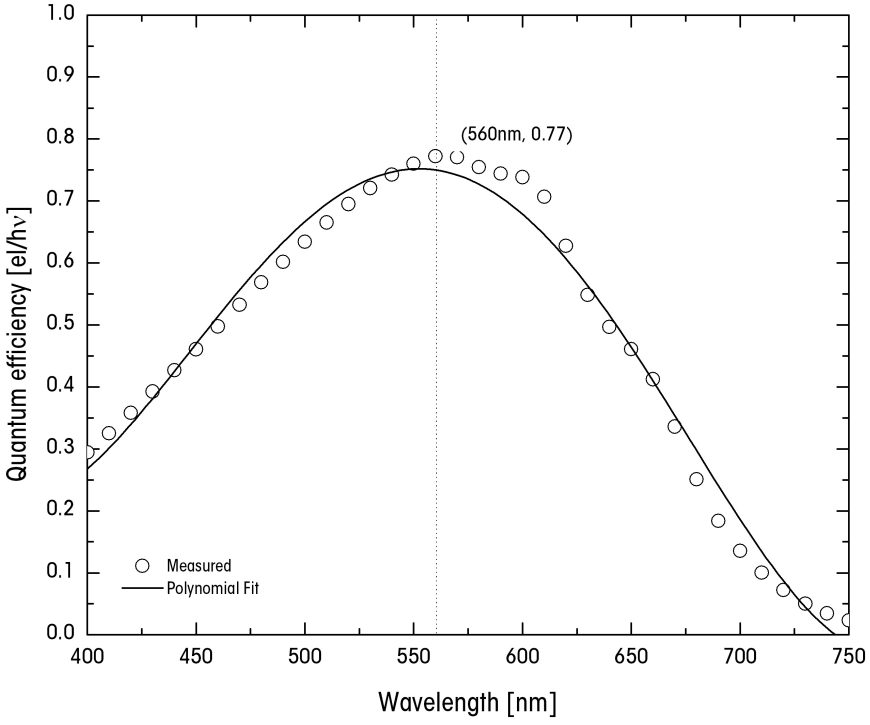

Figure 5.13: Measured quantum efficiency of the a-Si:H photodiode.

measures the fraction of the total variability in a data set that is accounted for by the model. The R^2 value is often quoted for fitted models, where high values of R^2 are deemed beneficial. In fact, the R^2 value was used during the fitting process to judge the fitness of the model. Unfortunately, a high value of R^2 does not guarantee a valid model. A better validation method is to use the residue, which was described at the beginning of this Chapter with Equation 5.1. This section determines how well the model fits the empirical data using the above method. The parameters extracted in Section 5.3 are applied to the equations presented in Chapter 4 and their residue are computed. If the model is correct, the residuals will approximate the statistical relationship between the model and empirical data. In other words, if the model fits, then the residue will be random. In the case that the residue is not random, the residue provides useful hints and information to improve the model further.

5.4.1 Current-Voltage Characteristics

The forward and reverse current-voltage characteristics will be validated separately, since they were modeled that way. The forward region was modeled by the sum of two weighted functions. The low forward bias region was modeled using the ideal diode equation, where the saturation current and ideality factor are temperature dependent. The high forward bias region was modeled using a power law relationship with temperature dependent saturation current and exponential. A weighting function was used to emphasize the effect of the appropriate function at the selected area and to allow for the smooth transition between the two curves. The reverse bias current includes several different components. The total reverse bias current is modeled as the sum of the bulk thermal current and the edge current component.

The bulk and edge components are bias and temperature dependent.

Forward Bias Photodiode Current

Using the parameters extracted in Table 5.5, the forward bias current characteristics of a 1×1 mm^2 n-i-p photodiode at 40 °C and its corresponding residue are calculated. The (a) predicted and measured current characteristics and (b) residues are shown in Figure 5.14. As can be seen, the residue follows a random pattern except for two locations: at the middle bias region (0.3 to 0.4 V) and at high biases. The deviation at the the middle bias region comes from the fitting function. At high biases, the residue seems large compared to other regions. However, the error is quite small relative to the magnitude of the modeled current. The residue at high bias shows that the modeled current underestimates the actual current. This fact can be explained by the fact that the model does not take into account contact injection. Other possible explanations for the possible discrepancies include measurement errors and curve fitting errors.

Reverse Bias Photodiode Current

The reverse bias current was modeled as the sum of the bulk component and the edge component. The bulk current has an exponential relationship to temperature and bias. The edge component also has a temperature and bias dependent, but the relationship is that of a quadratic. Seen in Figure 5.15 are (a) the reverse bias current characteristics of a 1×1 mm^2 n-i-p photodiode at 40 °C and (b) its corresponding calculated residue. The values were calculated using the parameters found in Table 5.6. Although it seems that the reverse bias current model fits the model well, the shape of the residual plot looks like a cubic polynomial, suggesting

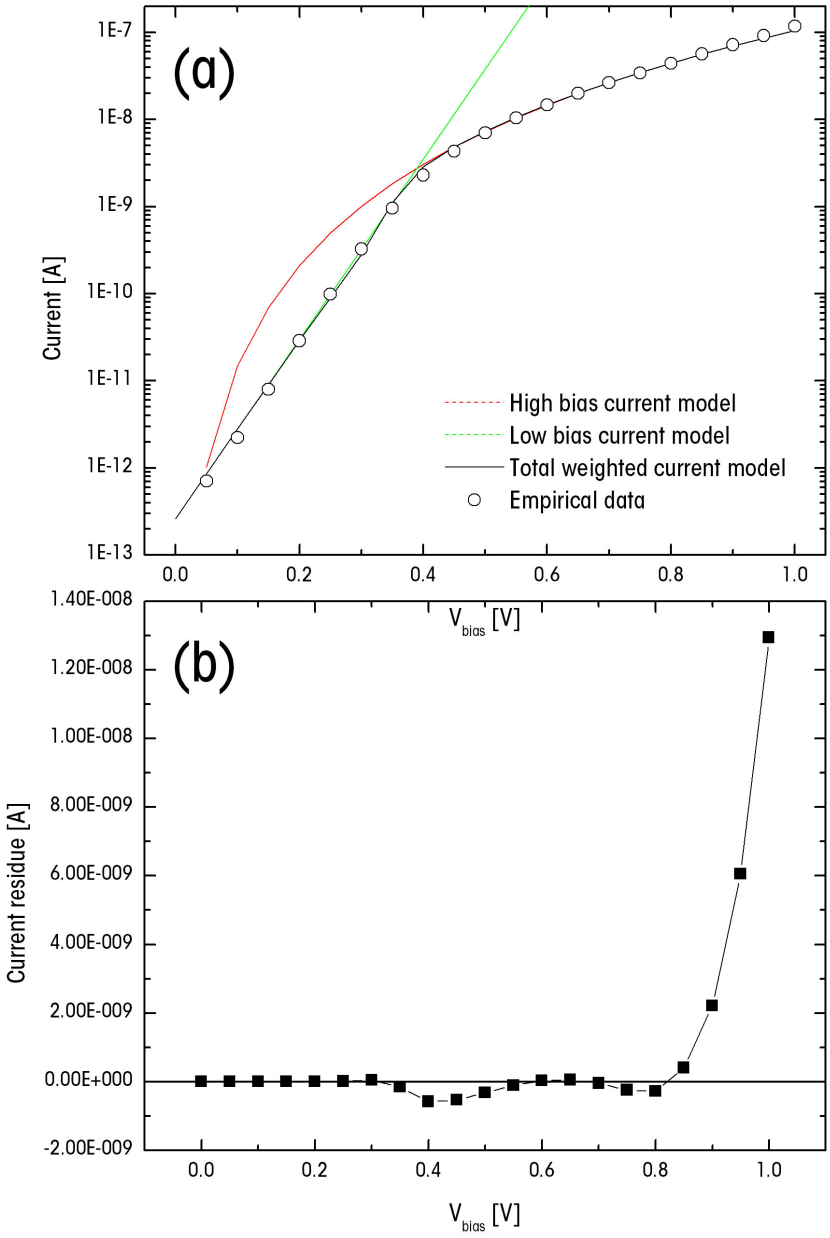

Figure 5.14: Graph showing the (a) calculated and measured forward current characteristics of a 1×1 mm^2 n-i-p photodiode at 40 °C and (b) the calculated residue.

that further improvement can be made. The residues for the edge and bulk components were extracted and it was observed that the error comes mainly from the edge component. This trend suggests that adding another term to the edge model polynomial might account for the structure left in the data by the quadratic. This process of residuals calculation and model fitting can be reiterated indefinitely with ever increasing degrees of polynomial. However, there is the problem that polynomial models become highly unstable as their degree increases. A different type of model, such as a nonlinear model or a LOESS model might be more suitable then [77].

5.4.2 Capacitance Characteristics

Figure 5.16 shows the calculated residuals for the capacitance based on the linear fit Equation 5.14. Unfortunately, it can be seen from the figure that the residue is non-random which implies that there is more than just a linear bias dependence affecting the capacitance. Pfleiderer et al. presented an alternative model for the capacitance of a a-Si:H n-i-p diode that suggests that there would be a correctional factor that has a hyperbolic tangent dependence to the Debye length and an inverse logarithmic dependence to the frequency [90]. However, Pfleiderer's model is computation intensive and requires the knowledge of the density of states of the intrinsic layer.

5.4.3 Illumination Response

Based on the parameters presented in Table 5.8, the residuals were calculated using equation 5.1 and plotted in Figure 5.17. As can be seen, other than a short

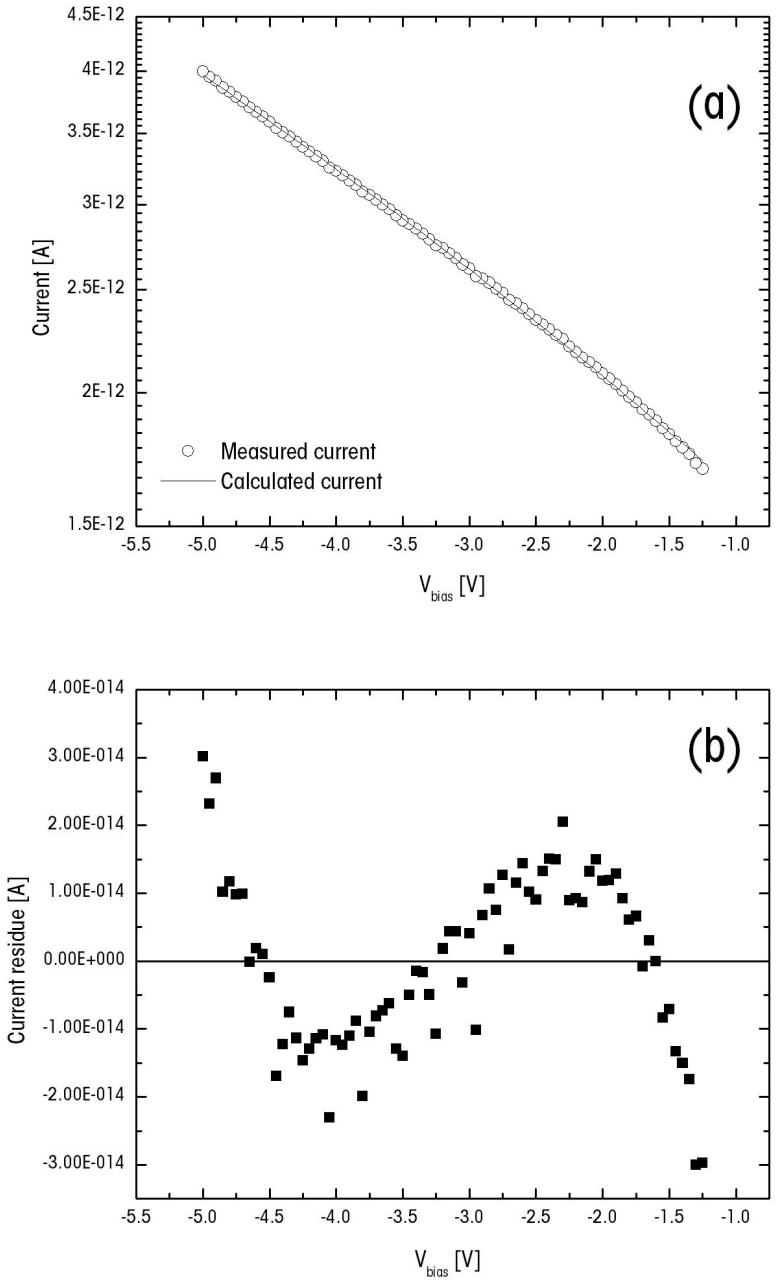

Figure 5.15: Graph showing the (a) calculated and measured reverse current characteristics of a 1×1 mm^2 n-i-p photodiode at 40 °C and (b) the calculated residue.

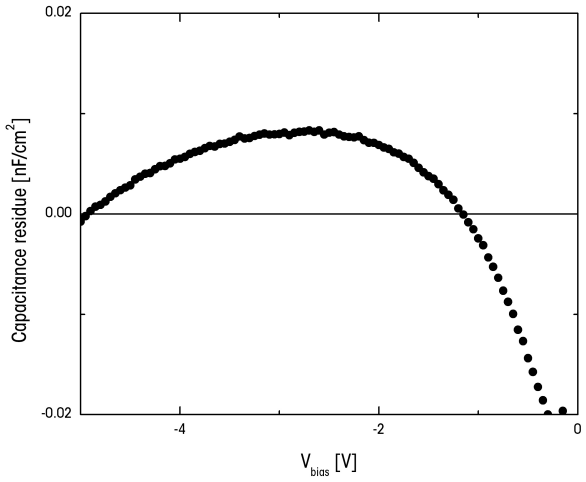

Figure 5.16: Scatter plot of capacitance residuals.

sinusoidal like behavior at low wavelengths, the residues tend to be fairly random. This randomness is desirable, as it implies that the model fits the data reasonably well. The residual sinusoidal detected can be attributed to the constructive and destructive interference caused by the top anti-reflection coating or by the indium tin oxide layer. In most quantum efficiency plots found in literature, there is often an observed sinusoidal pattern, as shown in Figure 5.18. A more accurate model will be to use transmittance and reflectance equations to include the interference caused by the top transparent layers.

5.5 Summary

This chapter validates the empirical model presented in the preceding chapter. First, a description of the devices under test is presented. Then, the different

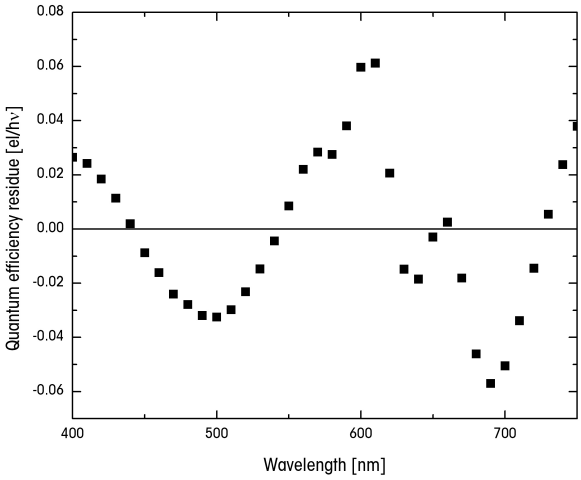

Figure 5.17: Scatter plot of quantum efficiency residuals.

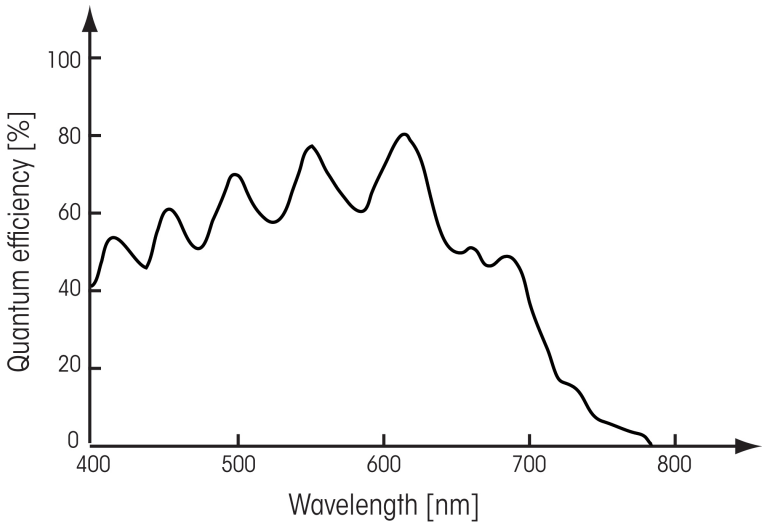

Figure 5.18: Quantum efficiency of a a-Si:H n-i-p photodiode as reported in literature [4].

measurement setups used to gather the experimental data were explained. The parameters for each equation were extracted by performing data reduction and curve fitting. The equations used for curve fitting are based on theoretical equations presented in Chapters 3 and 4. Finally, the model with the updated parameters was validated.

The validation step is a critical part of the whole model building process. The model is validated by calculating the residuals, which are the differences between the measured data and the calculated model. The forward bias current model fits the empirical data fairly well, but would benefit from a better weighting function and the inclusion of a contact injection model. As for the reverse bias current, the residue suggests that instead of using a quadratic function to fit the data, a cubic function or a non-linear function would be more suitable. The linear bias dependence of the capacitance was shown to be adequate, however by including a correctional factor it could be further improved. Finally, the illumination response or quantum efficiency model was evaluated. The fourth order model used to fit the quantum efficiency curve was deemed acceptable, except for low wavelengths, where a sinusoidal error was observed. The sinusoidal residue was attributed to the interference from the top transparent layers, and it was suggested to use optics equations to model the phenomenon. In short, the model fits the empirical data well, but requires further improvements in specific ranges of parameters.

Chapter 6

Conclusions and Future Work

An empirical model for segmented a-Si:H n-i-p photodiodes is presented. The model is described by a series of equations based on theoretical background as well as empirical results. The empirical data was obtained from a series of n-i-p samples fabricated at the Giga2Nano Laboratory. The equivalent circuit model of the photodiode is that of a diode shunted with a capacitor and a current source. The diode describes the current voltage characteristics of the photodiode. The capacitor and the current source account for the photodiode capacitance and the photocurrent respectively.

The forward bias current characteristics can be modeled as the weighted sum of an exponential low bias region and of a power law high bias region. The dark current can be modeled as the sum of the bulk thermal component and the edge leakage component. The bulk component equation is described by an exponential dependence on temperature from its thermal generation nature and by an exponential dependence on bias from its field enhanced generation characteristics. The thermal and bias dependence of the edge component were both modeled by quadratic equa-

tions. The capacitance of the photodiode was modeled as a linear bias dependent equation. Finally, the quantum efficiency, which determines the photocurrent, was modeled as a fourth order polynomial.

Possible future work will involve refinements of the model. A better weighting function needs to be used for the forward bias current characteristics. The forward bias current model also needs to account for additional components such as charge injection and the series resistance. In addition, further studies should be conducted to obtain a physical equation for the reverse edge leakage component. The capacitance model although adequate for the moment, could benefit from a frequency dependent correctional factor. The quantum efficiency model should take into account the optical behavior of the top transparent layers. Finally, additional study and analysis of the photodiodes in an array setting would be timely since the application of a-Si:H devices usually involves large area electronics. In that respect, additional study should also be conducted on the noise and switching performance of the device.

Bibliography

[1] R.A. Street. *Hydrogenated amorphous silicon*. Cambridge Solid State Science Series, 1991.

[2] J.H. Chang. Characterisation and modeling of a-Si:H nip photodiodes. Internal Technical Document, 2006.

[3] Y. Vygranenko, K.H. Kim, D. Striakhilev, J.H. Chang, and T.C. Chuang. Process development for a-Si:H nip photodiodes on glass and robust substrates. Internal Technical Document, 2006.

[4] R.A. Street, editor. *Technology and applications of amorphous silicon*. Springer, December 1999.

[5] S.S. Hegedus. Capacitance studies of a-SiGe: H pin solar cells. *Photovoltaic Specialists Conference, Conference Record of the Twenty First IEEE*, pages 1544–1549, 1990.

[6] R. A. Street. Thermal generation currents in hydrogenated amorphous silicon p-i-n structures. *Applied Physics Letters*, 57(13):1334–1336, 1990.

[7] N. Kramer and C. van Berkel. Reverse current mechanisms in amorphous silicon diodes. *Applied Physics Letters*, 64(9):1129–1131, February 1994.

[8] E.A. Schiff. Reverse bias currents in amorphous silicon nip sensors. *Journal of Non-Crystalline Solids*, 198-200:1155–1158, May 1996.

[9] J.H. Chang, T.C. Chuang, Y. Vygranenko, D. Striakhilev, K.H. Kim, A. Nathan, G. Heiler, and T. Tredwell. Temperature dependence of leakage current in segmented a-Si:H n-i-p photodiodes. *Material Research Society Symposium Proceedings*, To be published April 2007.

[10] J.H. Chang. Diode switched a-Si:H n-i-p photosensor array. Master's thesis, University of Waterloo, 2003.

[11] A. Catalano. *Amorphous and Microcrystalline Semiconductor Devices*. Artech House, April 1991.

[12] S. Qureshi, V. Perez-Mendez, SN Kaplan, I. Fujieda, G. Cho, and RA Street. Signal generation in a hydrogenerated amorphous silicon detector. *Nuclear Science, IEEE Transactions on*, 36(1):194–198, 1989.

[13] A.J. Snell, K.D. Mackenzie, W.E. Spear, P.G. LeComber, and A.J. Hughes. Application of amorphous silicon field effect transistors in addressable liquid crystal display panels. *Applied Physics A: Materials Science & Processing*, 24(4):357–362, 1981.

[14] N.M. Park. Band gap engineering of amorphous silicon quantum dots for light-emitting diodes. *Applied Physics Letters*, 78(17):2575, 2001.

[15] R.G. Neale and J.A. Aseltine. The application of amorphous materials to computer memories. *Electron Devices, IEEE Transactions on*, 20(2):195–205, 1973.

[16] R. Frigg and S. Hartmann. Models in science. In Edward N. Zalta, editor, *The Stanford Encyclopedia of Philosophy*. February 2006.

[17] G.A. Swartz. Computer model of amorphous silicon solar cell. *Journal of Applied Physics*, 53(1):712–718, January 1982.

[18] I. Chen and S. Lee. On the current-voltage characteristics of amorphous hydrogenated silicon Schottky diodes. *American Institute of Physics*, 53(2):1045–1051, February 1982.

[19] H. Okamoto, H. Kida, S. Nonomura, and Y. Hamakawa. Variable minority carrier transport model for amorphous silicon solar cells. *Solar Cells*, 8:317–336, 1983.

[20] R.S. Crandall. Modeling of thin film solar cells: uniform field approximation. *Journal of Applied Physics*, 54(12):7176–7186, 1983.

[21] I. Sakata and Y. Hayashi. Theoretical analysis of trapping and recombination of photogenerated carriers in amorphous silicon solar cells. *Applied Physics A: Materials Science & Processing*, 37(3):153–164, 1985.

[22] M. Hack and M.Shur. Theoretical modeling of amorphous silicon-based alloy p-i-n solar cells. *Journal of Applied Physics*, 54(10):5858–5863, October 1983.

[23] M. Hack and M. Shur. Physics of amorphous silicon alloy p-i-n solar cells. *Journal of Applied Physics*, 58(2):997–1019, July 1985.

[24] P. Sichanugrist, M. Konagai, and K. Takahashi. Theoretical analysis of amorphous silicon solar cells: effects of interface recombination. *Journal of Applied Physics*, 55(4):1155–1161, 1984.

[25] J.L. Gray. A computer model for the simulation of thin-film silicon-hydrogen alloy solar cells. *IEEE Transactions on Electron Devices*, 36(5), 1989.

[26] P. Suppes. A comparison of the meaning and uses of models in mathematics and the empirical sciences. *Synthese*, 12(2):287–301, 1960.

[27] H. Akaike. A new look at the statistical model identification. *IEEE Transactions on Automatic Control*, 19(6):716–723, 1974.

[28] M. Forster and E. Sober. How to tell when simpler, more unified, or less ad hoc theories will provide more accurate predictions. *The British Journal for the Philosophy of Science*, 45(1):1, 1994.

[29] M.S. Morgan and M. Morrison. *Models as mediators: perspectives on natural and social science*. Cambridge University Press, 1999.

[30] R.C. Chittick, J.H. Alexander, and H.F. Sterling. The preparation and properties of amorphous silicon. *Journal of the Electrochemical Society*, 116(1):77–81, 1969.

[31] P. G. Le Comber and W. E. Spear. Electronic transport in amorphous silicon films. *Physical Review Letters*, 25(8):509–511, August 1970.

[32] W.E. Spear and P.G. LeComber. Substitutional doping of amorphous silicon. *Solid state communications*, 88(11-12):1193–1197, 1975.

[33] N.F. Mott. Conduction in non-crystalline materials: Iii. localized states in a pseudogap and near extremities of conduction and valence bands. *Philosophical Magazine*, 19(160):835–852, 1969.

[34] A. Sazonov. Hydrogenated amorphous silicon fundamentals. Course Notes, 2002.

[35] J.D. Plummer, M.D. Deal, and P.B. Griffin. *Silicon VLSI Technology - Fundamentals, Practice and Modeling*. Prentice Hall Electronics and VLSI Series, 2000.

[36] D.K. Biegelsen, R.A. Street, C.C. Tsai, and J.C. Knights. Defect creation and hydrogen evolution in amorphous si:h. *Journal of Non-Crystalline Solids*, 35-36(1):285–290, January-February 1980.

[37] R.A. Street, J.C. Knights, and D.K. Biegelsen. Luminescence studies of plasma-deposited hydrogenated silicon. *Physical Review B*, 18(4):1880–1891, August 1978.

[38] S. Wang. *Fundamentals of semiconductor theory and device physics*. Prentice Hall Englewood Cliffs, 1989.

[39] S.R. Elliott. *Physics of amorphous materials*. Longman Scientific & Technical, 1983.

[40] P.W. Anderson. Absence of diffusion in certain random lattices. *Physical Review*, 109(5):1492–1505, 1958.

[41] K. Winer and L. Ley. Surface states and the exponential valence-band tail in a-Si:H. *Physical Review B*, 36(11):6072–6078, 1987.

[42] D.L. Staebler and C.R. Wronski. Reversible conductivity changes in discharge-produced amorphous si. *Applied Physics Letters*, 31(4):292–294, 1977.

[43] D.L. Staebler and C.R. Wronski. Optically induced conductivity changes in discharge-produced hydrogenated amorphous silicon. *Journal of Applied Physics*, 51(6):3262–3268, June 1980.

[44] M. Stutzmann, D.K. Biegelsen, and R.A. Street. Detailed investigation of doping in hydrogenated amorphous silicon and germanium. *Physical Review B*, 35(11):5666–5701, April 1987.

[45] D.V. Lang, J.D. Cohen, and J.P. Harbison. Observation of a reversible field-induced doping effect in hydrogenated amorphous silicon. *Physical Review Letters*, 48(6):421–424, 1982.

[46] D.E. Carlson and C.R. Wronski. Amorphous silicon solar cell. *Applied Physics Letters*, 28(11):671–673, June 1976.

[47] J. Beutel, H.L. Kundel, and R.L. Van Metter, editors. *Handbook of Medical Imaging Volume 1 - Physics and Psychophysics*. SPIE- The International Society for Optical Engineering, 2000.

[48] K. Tsuji, Y.Takasaki, T. Hirai, and K. Taketoshi. Impact ionization process in amorphous selenium. *Journal of Non-Crystalline Solids*, 144(1):94–96, 1989.

[49] M. Matsumura, H. Hayama, Y. Nara, and K. Ishibashi. Amorphous-silicon image sensor IC. *Electron Device Letters, IEEE*, 1(9):182–184, 1980.

[50] R. A. Street. Long-time transient conduction in a-Si:H p-i-n devices. *Philosophical magazine. B. Physics of condensed matter. Structural, electronic, optical and magnetic properties*, 63(6):1343–1363, 1991.

[51] S.M. Sze. *Physics of semiconductor devices*. Wiley, 1969.

[52] J. B. Johnson. Thermal agitation of electricity in conductors. *Physical Review*, 32(1):97–109, July 1928.

[53] H. Nyquist. Thermal agitation of electric charge in conductors. *Phys. Rev.*, 32(1):110–113, July 1928.

[54] K.H. Lundberg. Survey of noise sources in bulk CMOS (unpublished). October 2000.

[55] R. Sarpeshkar, T. Delbruck, and C. A. Mead. White noise in MOS transistors and resistors. *IEEE Circuits Devices Magazine*, pages 23–29, November 1993.

[56] J.B. Johnson. The Schottky effect in low frequency circuits. *Physical Review*, 26(1):71–85, July 1925.

[57] H.A. Watson. *Microwave semiconductor devices and their circuit applications*. McGraw-Hill Education, April 1969.

[58] A.L. McWhorter. 1/f noise and germanium surface properties. In R.H. Kingston, editor, *Semiconductor Surface Physics*, pages 207–228. University of Pennsylvania Press, Philadelphia, 1957.

[59] F.N. Hooge. 1/f noise is no surface effect. *Physics Letters A*, 29(3):139–140, April 1969.

[60] F.N. Hooge. Discussion of recent experiments on 1/f noise. *Physica*, 60(1):130–144, July 1972.

[61] F.N. Hooge and L.K.J. Vandamme. Discussion of recent experiments on 1/f noise. *Physics Letters A*, 66(4):315–316, May 1978.

[62] F.N. Hooge. 1/f noise sources. *IEEE Transactions on Electron Devices*, 41(11):1926–1935, November 1994.

[63] F.A. Bathaei and J.C. Anderson. Electrical noise measurements in intrinsic amorphous silicon. *Philosophical Magazine B*, 55:87–100, 1987.

[64] F.A. Bathaei and J.C. Anderson. Flicker noise in hydrogeneated amorphous-silicon schottyky diodes. *Philosophical Magazine B*, 57:259–269, 1988.

[65] G. Cho, S. Qureshi, J.S. Drewery, T. Jing, and S.N. Kaplan. Noise in a-Si:H p-i-n detector diodes. *IEEE Transactions on Nuclear Science*, 39(4):641–644, 1992.

[66] H. Wieczorek. Effects of trapping in a-Si:H diodes. *Solid State Phenomena*, 44-46:957–972, 1995.

[67] C.E. Parman, N.E. Israeloff, and J. Kakalios. Conductance fluctuations in doped hydrogenated amorphous silicon. *Physical Review B*, 47(19):12578–12589, May 1993.

[68] F. Blecher, B. Schneider, J. Sterzel, M. Hillebrand, S. Benthien, and M. Böhm. Noise analysis of imagers with a-Si:H pin diode pixels. *Journal of Non-Crystalline Solids*, 266-269:1188–1192, 2000.

[69] M.J. Thompson, N.M. Johnson, R.J. Nemanich, and C.C. Tsai. Silicide formation in pd-a-Si:H Schottky barriers. *Applied Physics Letters*, 39(3):274–276, August 1981.

[70] M. Hack and R.A. Street. Analysis of double injection transients in amorphous silicon p-i-n diodes. *Journal of Applied Physics*, 72(6):2331–2339, September 1992.

[71] J. Deng and C.R. Wronski. Carrier recombination and differential diode quality factors in the dark forward bias current-voltage characteristics of solar cells. *Journal of Applied Physics*, 98(2):24509–24509, 2005.

[72] T.R. Johnson, G. Ganguly, G.S. Wood, and D.E. Carlson. Investigation of the causes and variation of leakage currents in amorphous silicon p-i-n diodes. *Material Research Society Symposium Proceedings*, 762:A7.7.1–A7.7.6, 2003.

[73] M. Mulato, C.M. Hong, and S. Wagner. Size and etching effects on the reverse current of a-Si:H p-i-n diodes. *Journal of the Electrochemical Society*, 150(12):G735–G738, 2003.

[74] J.K. Arch and S.J. Fonash. Origins of reverse bias leakage currents in hydrogenated amorphous silicon p-i-n detector structures. *Applied Physics Letters*, 60(6):757–759, February 1992.

[75] A. Ilie and B. Equer. Field-enhanced generation in hydrogenated amorphous silicon. *Physical Review B*, 57(24):349–359, June 1998.

[76] J.K. Arch and S.J. Fonash. Using reverse bias currents to differentiate between bulk degradation and interfacial degradation in hydrogenated amorphous silicon p-i-n structures. *Journal of Applied Physics*, 72(9):4483–4485, 1992.

[77] Nist/sematech e-handbook of statistical methods. Online, http://www.itl.nist.gov/div898/handbook/, July 2006.

[78] Y. Vygranenko, J.H. Chang, and A. Nathan. Two-dimensional a-Si: H nip photodiode array for low-level light detection. *Quantum Electronics, IEEE Journal of*, 41(5):697–703, 2005.

[79] K.H. Kim, Y. Vygranenko, M. Bedzyk, J.H. Chang, T.C. Chuang, D. Striakhilev, A. Nathan, G. Heiler, and T. Tredwell. High performance hydrogenated amorhpous silicon n-i-p photodiodes on glass and plastic substrates by low-temperature fabrication process. *Material Research Society Symposium Proceedings*, To be published April 2007.

[80] Stanford Research Systems, Sunnycale, California. *Model SR830 DSP Lock-In Amplifier User Manual*, 2001.

[81] D.P. Blair and P.H. Sydenham. Phase sensitive detection as a means to recover signals buried in noise. *Journal of Physics E: Scientific Instruments*, 8:621–627, 1975.

[82] H. Matsuura, A. Matsuda, H. Okushi, and K. Tanaka. Dark current transport mechansim of p-i-n hydrogenated amorphous silicon didodes. *Journal of Applied Physics*, 58(4):1579–1583, August 1985.

[83] M. Hoheisel, E. Reichle, H. Harms, and J. Kotschy. Temperature dependence of the photocurrent in pin and nip solar cell structures made from a-Si:H. *Journal of Non-Cystalline Solids*, 137, 138:1181–1184, 1991.

[84] M. Lyakas, R. Zaharia, and M. Eizenberg. Analysis of nonideal Schottky and p-n junction diodes- extraction of parameters from IV plots. *Journal of Applied Physics*, 78(9):5481–5489, 1995.

[85] A. Ortiz-Conde, F.J. García Sánchez, J.J. Liou, J. Andrian, R.J. Laurence, and P.E. Schmidt. A generalized model for a two-terminal device and its applications to parameter extraction. *Solid State Electronics*, 38(1):265–266, 1995.

[86] J.C. Ranuarez, A. Ortiz-Conde, and F.J. García Sánchez. A new method to extract diode parameters under the presence of parasitic series and shunt resistance. *Microelectronics Reliability*, 40(2):355–358, 2000.

[87] H. Wong and WH Lam. A robust parameter extraction method for diode with series resistance. *Electron Devices Meeting, 2001. Proceedings. 2001 IEEE Hong Kong*, pages 38–41, 2001.

[88] J. Osvald and E. Dobrocka. Generalized approach to the parameter extraction from I-V characteristics of Schottky diodes. *Semiconductor Science Technology*, 11:1198–1202, 1996.

[89] J. Perrin and I. Solomon. Conductivity and Temperature Dependence of the Optical Gap in Hydrogenated Amorphous Silicon. *Journal of Non-Crystalline Solids*, 37(3):407–410, 1980.

[90] H. Pfleiderer and B. Rauscher. Capacitance of amorphous silicon pin solar cells. *Physica Status Solidi A*, 75:537–545, 1983.

Glossary

Notation	Description
C	Capacitance value.
E_{OC}	Slope of conduction band tail.
E_{OV}	Slope of valence band tail.
E_{μ}	Optical band gap.
E_{F}	Fermi energy level.
G	Optical excitation rate.
J_n	Electron current density.
J_p	Hole current density.
N_D	Defect density.
$N_{ct}(E)$	DOS distribution for the conduction band tail.
$N_{vt}(E)$	DOS distribution for the valence band tail.
P	Fraction of charge collected.
R	Load resistance.
R_S	Series resistance.
T	Temperature.
U	Defect states correlation energy, the difference in energy levels between D^- and D^0 states.
V_{bias}	Bias voltage.
V_{bi}	Internal built-in potential in the n-i-p photodiode.
$[H]$	Hydrogen content.
Δf	Bandwidth over which the noise is measured.
α_H	Hooge's constant.
η_{QE}	Quantum efficiency.
λ	Wavelength of illumination.
λ_{Diff}	Carrier diffusion length.
μ_{De}	Mobility of free electron.

Notation	Description
μ_{Dh}	Mobility of free holes.
μ_n	Electron drift mobility.
μ_p	Hole drift mobility.
σ	Conductivity.
$\sigma_{Extended}$	Conductivity in the extended state.
$\sigma_{Hopping}$	Conductivity due to hopping from deep states.
$\sigma_{Localized}$	Conductivity in the localized state.
σ_c	Trapping cross-section.
$\sigma_{intrinsic}$	Intrinsic a-Si:H Conductivity.
σ_{n+}	n+ a-Si:H Conductivity.
σ_{p+}	p+ a-Si:H Conductivity.
τ	Carrier lifetime.
τ_F	Thickness of the device.
τ_e	Recombination lifetime of free electrons.
τ_h	Recombination lifetime of free holes.
a_E	Mean free path of carriers.
d	Thickness of the i-layer.
f_p	Scaling parameter for the weighting function.
f_q	Center parameter for the weighting function.
k	Boltzmann's constant. Physical constant relating temperature to energy and has a value of $8.617343(15) \times 10^{-5}$ eV·K^{-1}.
n	Electron concentration.
p	Hole concentration.
q	Elementary charge. The charge carried by a single proton and has a value of $1.60217653(14) \times 10^{-19}$ C.
w_1	Activation energy for hopping.
w_2	Hopping energy for deep states.
a-Si	Non-hydrogenated amorphous silicon.
a-Si:H	Hydrogenated amorphous silicon.
AC	Alternate current.
Al	Aluminium.
Ar	Argon.
c-Si	Crystalline silicon.

Notation	Description
Chalcogen	Materials composed of a chalcogen and a more electropositive element. Chalcogens are elements from the periodic table group 16 which include oxygen (O), sulfur (S), selenium (Se), tellurium (Te), the radioactive polonium, (Po), and the synthetic ununhexium (Uuh).
CPM	Constant photocurrent method.
Cr	Chromium.
CVD	Chemical vapor deposition.
D^+	Positively charged defect state, a dangling bond that lacks an electron.
D^-	Negatively charged defect state, a dangling bond that has an extra electron.
D^0	Neutral charged defect state.
DNA	Deoxyribonucleic acid is a nucleic acid that contains the genetic instructions for the development and functioning of living organisms.
DOS	Density of states.
DUT	Device under test.
ESR	Electron spin resonance.
Glow discharge	Type of plasma formed by passing a current through a gas.
i-layer	Intrinsic a-Si:H layer.
IC	Integrated circuit.
ITO	Indium tin oxide.
KVL	Kirchoff's voltage law.
LED	Light emitting diode.
MIS	Metal-insulator semiconductor.
Mo	Molybdenum.

Notation	**Description**
Passivation	Process of making a material less reactive with respect to another material.
PDS	Photodeflection spectroscopy.
PECVD	Plasma enhanced chemical vapor deposition.
PF	Poole-Frenkel emission.
PH_3	Phosphine.
PSD	Phase sensitive detection.
RF	Radio frequency.
RIE	Reactive ion etching.
RMS	Root mean square.
SiH_4	Silane.
SRH	Shockley-Read-Hall.
TAT	Thermally assisted tunneling.
TCO	Transparent conductive oxide.
TFT	Thin film transistors.
TMB	Tri-methly boron.
WKB	Wentzel-Kramers-Brillouin.